JAYCOR

The Development of Biomechanically-based Criteria of Rib Fracture from KE-NLW Impact

Final Report J3194-03-202

Prepared by:
Weixin Shen, Ph.D.
Eugene Niu, Ph.D.

Jaycor, Inc.
3394 Carmel Mountain Road
San Diego, California 92121

Prepared for
Director
Joint Non-Lethal Weapon Directorate
Quantico, Virginia

Under contract No. DSC0239

August 2003

Executive Summary

Fracture of ribs is frequently observed in the application of kinetic nonlethal weapons (KE-NLW) and tends to cause severe trauma and even lethality. This is due to the fact that the chest is very likely to be hit and many vital organs exist inside the chest wall. A recent animal study of human effects of KE-NLW conducted at the Walter Reed Army Institute Research (WRAIR) also showed that rib fracture was among the leading thoracic injury modes that occurred from KE-NLW impacts. There currently exists no criterion for predicting the potential of rib fracture under KE-NLW impacts. The criterion developed for thoracic injury prediction under car crash conditions, the so-called viscous criteria (VC), did not work for KE-NLW impacts when validated against the WRAIR animal test data. This can be explained by the fact that VC is an empirical criterion that is based on animal tests using impactors that were much heavier but slower than NLW. Therefore, there is clearly a need for developing a biomechanically-based criterion for predicting the potential of rib fracture under KE-NLW impacts.

Biomechanically-based rib fracture criteria were developed in this study for high-speed impacts. This work is made possible by several other studies: an ongoing animal study conducted jointly by Jaycor and the University of California at San Diego (UCSD), a completed animal study at WRAIR, and an ongoing work of developing subject-specific FEM of animal and human subjects at Jaycor.

First, a detailed finite element model (FEM) of ribs was developed. This rib FEM was based on geometry constructed from high-resolution CT images. CT numbers were used to determine the density and elastic modulus of each pixel. Different material parameters were assigned to a corresponding element, therefore, this was a detailed 3D inhomogeneous FEM. To reduce the computational cost, several beam formulations were developed to convert the complex inhomogeneous rib structure into equivalent beam models that respond the same under the impacts. Each beam node was assigned material parameters determined from the material distribution in the rib cross section it represented, therefore, the beam FEM was also inhomogeneous. Extensive numerical study was conducted and it was concluded that the beam FEM was far more efficient numerically and was at least as accurate as a very finely meshed 3D rib FEM. The rib FEM was then implemented into the subject-specific swine thoracic FEM models that were also constructed from CT images. After being calibrated against the response measurements from the Jaycor/UCSD tests, the finite element models were used to simulate the Jaycor/UCSD tests and the WRAIR animal tests using both sponge grenades and steel balls. Model calculations of the peak motion responses, internal forces, and a number of stress and strain-based quantities for each rib were correlated to rib fracture potential using logistical

regression. Statistical analysis indicates that the stress-based criteria correlate much better to the data than the motion responses and internal forces. This conclusion is intuitive since the fundamental mechanism of rib fracture is that the stress exceeds the strength of the rib bone. There is no significant difference among various stress-based variables. However, strains are not as good correlates as stresses. In addition, in contrast to car crash impacts where chest deformation is believed to be a good correlate, peak rib deformation is not a good correlate under high-speed, lower-mass impact conditions.

Correlation curves using stresses as correlates were developed and are provided in the report. The correlations fitted the animal test data very well and the threshold values are consistent with bone strength data found in the literature. The FEM modeling of rib can be easily incorporated into a human thoracic FEM to predict bone stresses under impact. And since the injury correlations represent the fundamental relationship between bone stress and strength, it is believed to be valid for humans.

FORWARD (2018)
This document from 2003 is one of the earlier technical reports from the Joint Non-Lethal Weapons Program efforts in the area of blunt impact injury finite element modeling. This research and development has continued in earnest since then to present day. Many milestones have been achieved along the way and the DoD's blunt impact injury modeling capabilities have played a major role in allowing less injurious non-lethal weapons projectiles to be designed and fielded. As evident in the description in the introduction and executive summary of this document there was a need to ensure that the potential for significant injury is minimized moving forward. Improved materials, projectile design, and better information on the potential risks of injury in different operational scenarios, all which have been aided by the modeling capability, have led to a reduction in the risk of significant injury of non-lethal blunt impact capabilities. Although much has been learned and improved upon since 2003, the risk of injury from blunt impact projectiles is still a focus area of research and development for the JNLWP. The base rate of significant injury is low, however, amongst the injuries that do occur rib fractures are a major component. As such, the JNLWP continues to pursue improvements in the DoD's ability to accurately predict torso injuries including rib fracture.

Joint Non-Lethal Weapons Directorate, Human Effects Office, August 2018

Contents

List of Figures

List of Tables

1. Overview

1.1 Introduction

Fracture of ribs is frequently observed in the application of kinetic nonlethal weapons (KE-NLW) and tends to cause severe trauma and even lethality. This is due to the fact that the chest is the location very likely to be hit and many vital organs exist inside the chest wall. A recent animal study of human effects of KE-NLW conducted at the Walter Reed Army Institute Research (WRAIR) also showed that rib fracture was among the leading thoracic injury modes that occurred from KE-NLW impacts.

Under the sponsorship of JNLWD, Jaycor has developed and improved the Interim Total Body Model (ITBM) to provide an estimate of the injuries that could result from the impact of kinetic nonlethal weapons (Stuhmiller *et al.* 1996). Since there existed no criterion for predicting the potential of rib fracture under KE-NLW impacts, the injury criteria for rib fracture currently adopted in ITBM was the so-called viscous criteria, VC, that appeared in the literature as a proposed correlate. However, when validated against the WRAIR animal data, VC significantly underestimated the potential for rib fracture. Therefore, it is necessary to develop a rib fracture criteria that is based on the actual biomechanical responses of ribs at the local level.

Two aspects were addressed in this research: developing a detailed finite element model of ribs and surrounding tissues, and developing an injury criteria that correlate the biomechanical responses predicted from the model to the potential of rib fracture. On the modeling side, a detailed three-dimensional finite element model (FEM) of rib was developed. The bone material property was directly determined from CT images and different values were assigned to different elements. Therefore, it was an inhomogeneous FEM that accurately represented the rib as a composite structure. To reduce the computational cost, beam formulations were developed so that ribs were also modeled by an inhomogeneous beam FEM that responded equivalently as the more complex 3D FEM. Extensive numerical studies showed that the beam FEM was at least as accurate as the 3D FEM and was far more efficient numerically.

To develop biomechanically-based injury correlation, the beam FEM of ribs was incorporated into the existing swine thoracic FEM, which had accurate anatomical geometries that were reconstructed from medical images and material parameters calibrated against animal test data. The FEM was then used to simulate the WRAIR animal study to predict stresses in ribs during the impacts. Model calculations of the peak motion responses, internal forces, and a number of

stress and strain-based quantities for each rib were correlated to rib fracture data by the method of logistical regression. Statistical analysis was then used to determine the correlates that best fit the test data. And finally the correlation curves were developed.

The organization of this report is as follows. This chapter gives a brief review of the mechanisms of rib fracture, available human and animal data of rib fractures from KE-NLW impacts, and the validation of current rib fracture criteria against the animal test data. In the second chapter, detailed 3D inhomogeneous FEM of rib and beam FEM of rib are developed from medical images, and numerical studies are conducted to determine the performance of the models. The beam FEM of rib is then assembled into the existing thoracic swine FEM in the third chapter. In the fourth chapter, numerical simulations of animal tests are conducted, statistical analysis is then performed based on the FEM calculations and animal test data, and finally injury correlations using the best correlates are developed.

1.2   Rib Fracture Data

Most of the nonlethal weapons that are being used are kinetic types of weapons. They rely on the kinetic energy of the projectile to decapacitate the subject while not kill or severely injure the subject. Since thorax and abdomen are the areas that are mostly to be hit, it is not surprising that rib fracture is one of the leading injuries that can be caused by the impact of KE-NLW. Although the fracture of an isolated rib is usually not severe, under high-speed ballistic impact, a fractured rib may penetrate the pleural wall, causing pneumothorax or hemothorax, or even penetrate the heart directly.

The National Institute of Justice (NIJ) sponsored a research to study the field use of non-lethal weapons in the US. Klinger *et al.* (2000) reported the collection and the analysis of 371 incidents where officers fired 967 impact projectiles. Most of the projectiles used were 12 gauge beanbag rounds and plastic baton rounds. Despite the difficulty of interpreting field data, it clearly shows that rib fracture is among the major thoracic injuries that can lead to severe injuries or even death. Among 145 impacts on the chest, 6 impacts caused the fracture. Among 253 impacts on the lower thorax and abdomen, 9 caused fractures. There were two cases where the subjects' deaths were caused by fractured ribs penetrating the subjects' lung and heart. This was a significant percentage considering that there were only 8 subjects killed.

A retrospective study by Mahajna *et al.* (2002) of the use of rubber bullets during the Israeli-Arab conflict reported 8 rib fractures out of 39 chest injuries. Two cases were moderate injuries and six cases were severe injuries. Retrospective studies of plastic bullet induced injuries in Northern Ireland (Steele *et al.* 1999) also showed that rib fracture should be a serious concern in using kinetic types of nonlethal weapons.

The US Army Land Warfare Laboratory conducted an extensive study in the early seventies (Shank 1974) using a variety of projectiles to impact animal subjects of a number of species. Rib fracture was a major injury observed. Bir (2000) also reproduced rib fractures in human cadavers using the projectiles that simulate the NLW impacts.

Walter Reed Army Institute of Research conducted a series of tests on swine. So far this is the most carefully designed test to study the effects of nonlethal weapons. Two types of projectiles were used in the tests, a sponge grenade that was about 4 cm in diameter and weighed about 28 grams, and a rubber covered steel ball that was about 1.8 cm in diameter and weighed about 18 grams. A total of 52 tests were conducted impacting the animals' chest, sternum and abdomen, including 35 thoracic impact tests with 12 using sponge grenades and 23 using rubber covered steel balls. For each test, the impact velocity was measured, a high-speed movie of the impact was recorded, and a detailed pathological study was conducted after the animal was sacrificed to provide comprehensive injury information. Four subjects had two fractured ribs among 12 sponge grenade tests. Among 23 steel ball impacts, 8 subjects had a single rib fracture. In almost all the cases, the fractures occurred right underneath or very close to the impact spots.

1.3   Rib Fracture Correlation and Mechanism

There is no correlation that is specifically developed to predict rib fracture under high-speed KE-NLW impacts. On the other hand, a significant amount of research has been conducted on the thoracic injuries during car crash impacts. It is generally accepted that rib fractures are related mostly to the deformation of the chest wall during car crash. Based on some earlier animal and cadaver test results (Kroell *et al.* 1981; Patrick *et al.* 1975), the so called viscous criteria, VCmax, which is the maximum value of the chest wall velocity multiplied by the chest wall deformation, was developed (Lau *et al.* 1986; Viano *et al.* 1988) and has been accepted as a good correlate to thoracic injuries in front car crashes. Some research work attempted to apply this correlation to predict rib fractures under KE-NLW impacts. Bir (2000) developed a "3-rib ballistic impact dummy" that was modified from an automobile crash dummy to match the cadaver response under the sternal impacts of several projectiles that simulated the NLW impacts. The dummy was used in ballistic tests and the measured dummy response was used to calculate the VCmax based upon which probability of thoracic injuries, including rib fractures, were estimated (DuBay *et al.* 1998; Lyon *et al.* 1999). However, the VCmax criterion is an empirical relationship that was specifically developed from tests that simulated the front car crash impacts. The impact velocity was significantly lower than the NLW. The projectiles are also lighter and the impact locations are far more versatile than simply frontal sternum impacts. Therefore, VCmax cannot be applied for NLW without validation.

A detailed analysis was conducted using WRAIR animal test data and the thoracic response model in ITBM (Stuhmiller *et al.* 1996). VCmax was calculated for each test and correlated to VCmax. The result indicated that the VCmax correlation developed for car crash predicted almost no rib fractures while in the real tests a significant number of fractures occurred. This suggests that the VCmax is not a good correlate to predict rib fracture under NLW impacts. The disagreement is not surprising considering that VC was taken from a limited number of experiments conducted by the automobile industry and does not have a clear biomechanical basis. In fact, it is well known that rib fracture is caused by excessive deformation gradient of the quasibrittle material to the point that local stresses or strains exceed critical values. In addition, automobile impacts involve significant larger masses and lower velocities than nonlethal weapon impacts, therefore, VC predicts injuries from the global motion of the whole rib cage. In KE-NLW impacts, it is clear from photographic data and simulations that local deformation takes place leading to the high strain and resulting fracture. This was clearly shown in WRAIR animal test data where most rib fractures occurred near the point of impact. VCmax implicitly reflects the rib fracture mechanism under the large mass low velocity front impact conditions, but it fails to reflect it under NLW impact conditions.

The fundamental mechanism of rib fracture, in the continual mechanics sense, is that the bone tissue stresses developed under impact exceeds the strength of the tissue, which represents the capability of the bone tissue to withstand the load. During front car crash, ribs are allowed to deform and bend significantly. The maximum stresses happen along the side of the ribcage where maximum bending occurs. As a result rib fractures from car crash usually occur away from the impact location. But it is very different in a NLW impact, the projectile is much smaller and the impact velocity is much higher. There is no significant deformation away from the impact location since the impact is more concentrated and the duration is short. As a result, peak stresses are expected to happen directly underneath the impact location due to the local bending or shearing. This was confirmed by the WRAIR test results that rib fractures almost always occurred at or very close to the impact location and started from the posterior (internal) side of the rib.

2. FEM of Rib

2.1   Rib Geometry

2.1.1   Geometrical Reconstruction & Volume Representation of Rib

A commercial software, 3D-Doctor, was used to obtain the geometry. The general procedure of the geometrical reconstruction is summarized here. First, image segmentation is conducted to create "boundaries" on each CT image that separate the ribs from the surrounding tissues (Figure 1). Second, corresponding boundaries from each image are connected into discrete surfaces as a collection of polygons representing the outer surfaces of the ribs. And finally, volume representation of ribs is created from the surfaces and the original DICOM files. In volume representations, each rib is saved as a collection of pixels with coordinates and CT numbers. Figure 2 gives the volume representation of the right 3rd rib constructed from the Visible Man data set (Ackerman 1991).

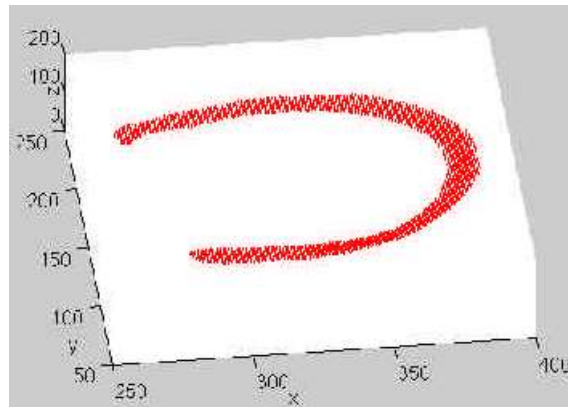**Figure 1. Geometrical reconstruction of ribs from the Visible Man dataset.**

Figure 2. Volume representation of the right 3rd rib of the Visible Man.

5

2.1.2 Geometrical Centerline of Ribs

The geometrical centerline of a rib is obtained in several steps. First, centers of mass of the rib are calculated on each image and connected to form the initial centerline. The rib volumes are then transferred from the global coordinate systems into the local coordinate systems that follow the initial guess of the centerline. The rib is then separated into a number of pieces that are perpendicular to and equally spaced along the initial centerline. The centers of mass are calculated for all the pieces. Three polynomial fittings of the centers of mass lead to a refined centerline. The rib is then separated into finer pieces along the refined centerline and the centers of mass are recalculated. Several iterations of the procedure produce a highly accurate centerline of the rib. Figure 3 shows the estimated centerline of the right 3rd rib from the Visible Man data set.
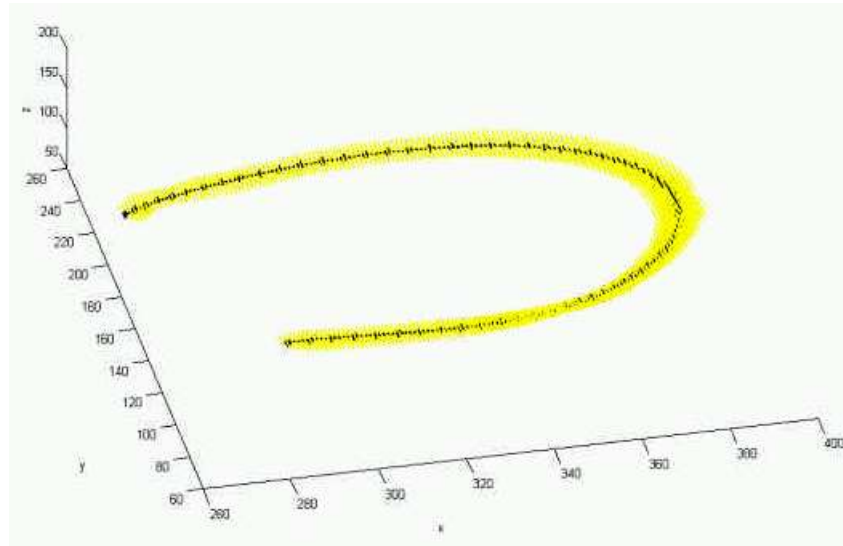
Figure 3. Estimated centerline of the right 3rd rib of the Visible Man.

2.1.3 Geometry Properties of Rib Cross Sections

After the centerline is obtained for a rib, geometrical properties of each rib cross section can be obtained. For a specified cross section that is normal to the centerline, the exterior boundary can be estimated from the raw coordinates. Using optimal fitting of the boundary, the cross section is then represented approximately by an ellipse (Figure 4), which has been demonstrated by Roberts *et al.* (1972). This simplifies the geometry property of the cross section into a few parameters: the long and the short axes and their orientation in the global coordinate system. Figure 4 shows the elliptical representation of a cross section of the rib. For all cross sections, the principal axes and orientations of ellipses can also be smoothed. Figure 5 gives the principal axes along the 3rd rib of the Visible Man. The results are consistent with that reported by Roberts *et al.* (1972), Schultz *et al.* (1974), and Minotti *et al.* (1991). Therefore, the geometry

6

properties of the rib include the centerline, principal long and short axes of each cross section and their orientation (Figure 6).
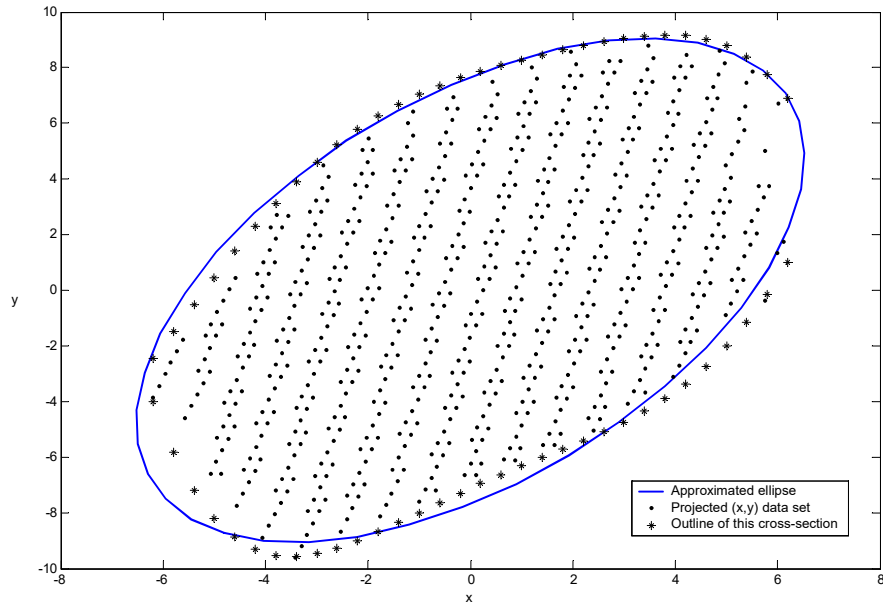
Figure 4. The ellipse approximation for the cross section.
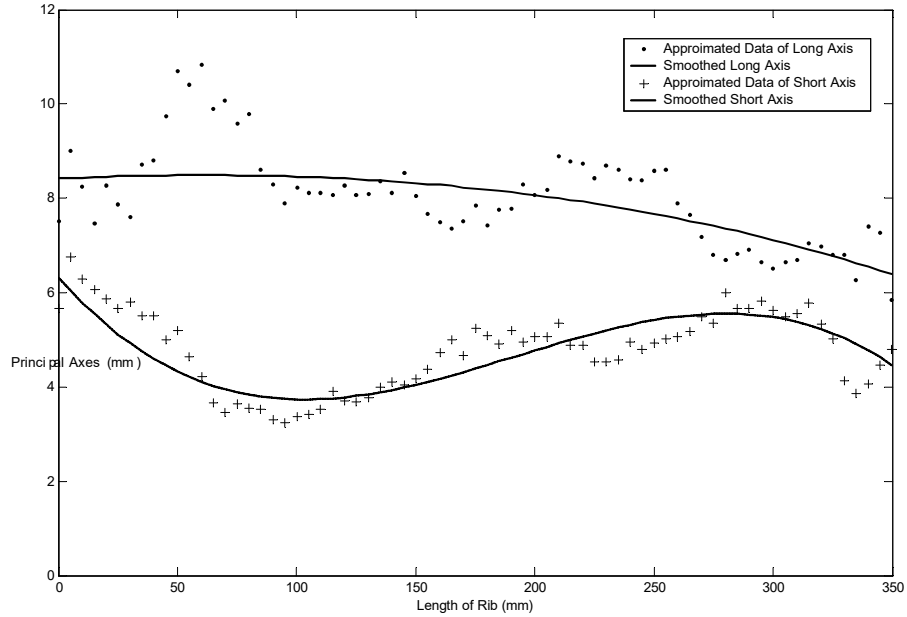
Figure 5. Principal half axes of ellipses for cross section of 3rd rib.
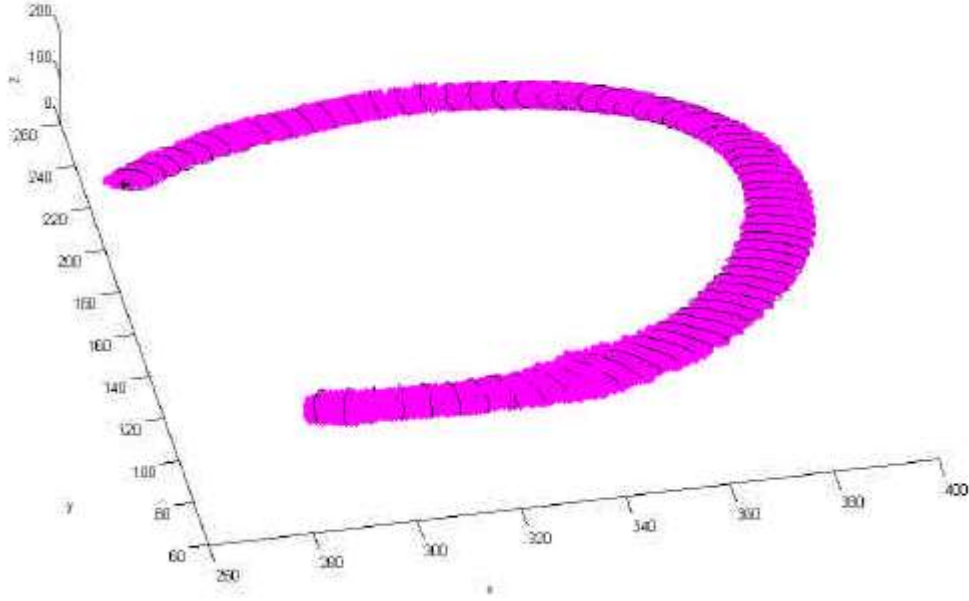
Figure 6. Geometry of the right 3rd rib of the Visible Man.

2.2 Material Properties of Human Ribs

The bone material properties can be obtained directly from the CT images in two steps. First, the CT number of each pixel is used to determine the density of the bone using the following linear relationship

$$\rho_{eff} = A * HU + 1000 (kg/m^3)$$

where ρ_{eff} is the effective density, HU is the Hounsfield unit (CT number), and A is a corrected factor that may depend on the CT machine. A is reported to be 0.523 by Rho *et al.* (1995), and 0.464 by Taylor *et al.* (2002). The elastic modulus can then be estimated from the effective density from equations obtained in literature. For general bone, Carter *et al.* (1977) reported the following relationship

$$E = 2875\rho^3 (Mpa) \quad (\rho \leq 2.0 g/cm^3)$$

Goldstein *et al.* (1991) used the following relationship that works for both cortical and trabecular bones

$$E = \begin{cases} 1352\rho^{1.48} & (MPa) & 0 \leq \rho < 1.4(g/cm^3) \\ 34623\rho - 46246(MPa) & 1.4 \leq \rho < 2.0(g/cm^3) \end{cases}$$

In addition, for cortical bones, the most used values for modulus are between 16 to 20 GPa. Couteau *et al.* (1998) reported density of 1996 kg/m^3 and elastic modulus of 16.7 GPa for cortical bones.

For trabecular bones, Hodgskinson *et al.* (1990) gives the range of modulus as a function of bone density as

$$E_{low} = 10^{(-4.10+2.47\log\rho)}$$
$$E_{mean} = 10^{(-2.43+1.96\log\rho)}$$
$$E_{high} = 10^{(-1.46+1.66\log\rho)}$$

in which modulus is in MPa and density is in kg/m^3. The range of trabecular bone modulus is also reported to be 0.4~3.6 GPa by Ryan *et al.* (1989), 3.81~5.72 GPa by Choi *et al.* (1992), and 2.23~10.1 GPa by Van Rietbergen *et al.* (1995).

The summary of the density versus modulus relationship is depicted in Figure 7. The relationship of Goldstein *et al.* (1991) is adopted here since it works for both cortical and trabecular bones.
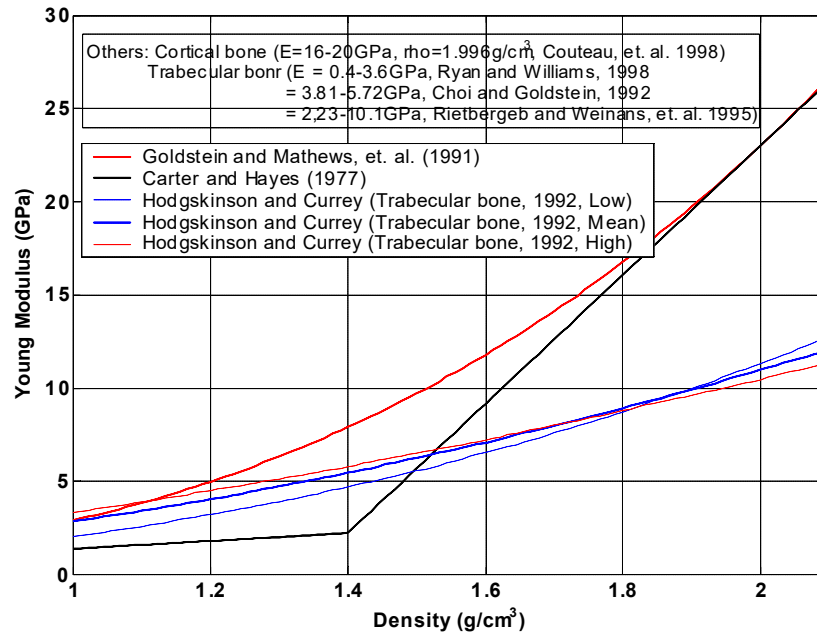
Figure 7. Summary of relationship between bone density and Young's modulus.

2.3   3D FEM of Rib

A detailed three-dimensional FEM is created based on the determined geometry and material properties from CT images. The finite element mesh is created based on a mesh template controlled by a set of parameters that can be easily adjusted to achieve different fineness of the mesh. For each element, material property including density and modulus is estimated as the average value of all the pixels the element covers. Figure 8 shows the 3D FEM for the right 3rd rib of the Visible Man, with different colors of elements indicating different values of density.
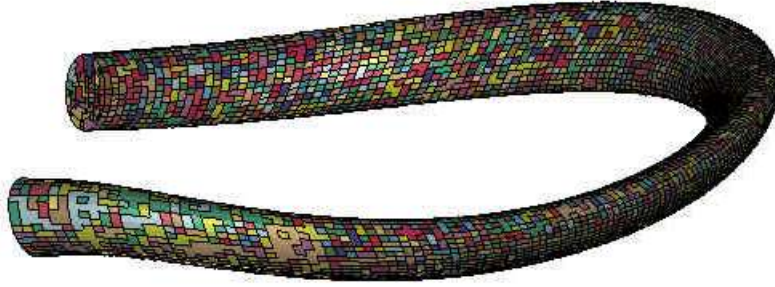
Figure 8. 3D FEM of the right 3rd rib of the Visible Man.

2.4   Beam FEM of Rib

In transient dynamical analysis, the computational cost is determined by both the size of the model (number of nodes) and the size of time step. The time step decreases with the decrease of element size and the increase of acoustic speed of material in the element. Bone has a high modulus and thus high wave speed. In addition, the characteristic dimension of rib is also very small, leading to both the large number of nodes and the small time step. Therefore, a detailed 3D FEM of rib is computationally expensive. To reduce the computational cost, two beam formulations of rib are developed.

2.4.1   Classical Beam Theory

When modeled as a beam structure, a beam node represents a specific cross section of the rib. The beam properties of a node include line density ρ_L, homogenized tensile stiffness <EA>, homogenized flexural stiffness along the principal axes, <EI$_x$> and <EI$_y$>, and homogenized torsion stiffness <GJ>. Based on the classical beam theory, these beam properties can be obtained from the distribution of density $\rho(x,y)$ and elastic modulus $E(x,y)$ in the cross section (Figure 9) as follows
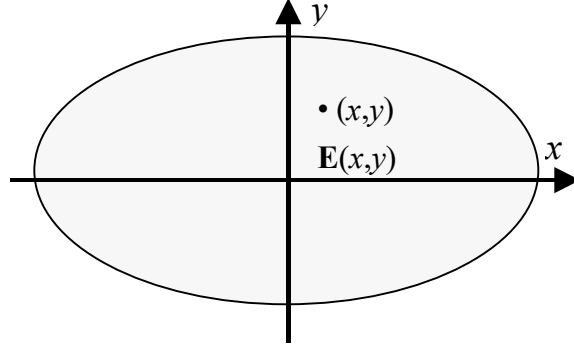
Figure 9. Density and Young's modulus as a function of (x,y).

$$\rho_L = \iint_S \rho(x,y)dxdy$$

$$<EA> = \iint_S E(x,y)dxdy$$

$$<EI_x> = \iint_S E(x,y)y^2dxdy$$

$$<EI_y> = \iint_S E(x,y)x^2dxdy,$$

$$<GJ> = \iint_S G(x,y)(x^2+y^2)dxdy$$

where υ is the Possion's ratio and $G = \dfrac{E}{2(1+v)}$.

The neutral lines are calculated by

$$\overline{x} = \frac{\iint_S E(x,y)xdxdy}{\iint_S E(x,y)dxdy}, \quad \overline{y} = \frac{\iint_S E(x,y)ydxdy}{\iint_S E(x,y)dxdy}$$

For a typical cross section of a rib, the values of $(\overline{x}, \overline{y})$ are very small. The geometrical central point can be used to form the neutral line of the beam.

The classical beam formulation assumes that the centerline of a rib cross section stays straight during the deformation and that the displacement fields are uncoupled along two principal axes.

11

2.4.2 Formulation Based on FEM Equivalency

To remove the assumption that the centerlines have to stay straight during deformation, another method is used. A FEM is developed of a long straight beam by extruding a specified cross section along the longitudinal direction. Material properties are the same in the longitudinal direction but vary within the cross section. One end of the straight beam is fixed and three types loads, tension, bending, and torsion, are applied on the other side. To avoid any boundary effects, the length of beam is chosen to be 8-10 times the size of the cross section. The FEM mesh and the three loading cases are depicted in Figure 10.
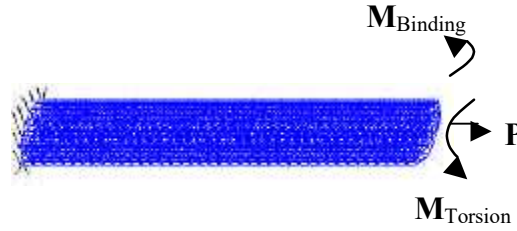
Figure 10. FEM of straight beam.

In this approach, the assumption of displacement fields being uncoupled along two principal axes is also removed by using the following displacement field (Estivalezes *et al.* 2001)

$$u = u_0(z) - y\theta_z(z) + k(x, y)$$
$$v = v_0(z) + x\theta_z(z) + h(x, y)$$
$$w = w_0(z) - x\theta_y(z) + y\theta_x(z) + g(x, y)$$

where g(x,y) is the out-of-plane warping function, k(x,y) and h(x,y) are two in-plane warping functions. Under different loadings, P, M_x, M_y, M_r the derivatives of displacements can be obtained as

$$\frac{\partial u}{\partial z} = \frac{du_0}{dz} - y\frac{d\theta_z}{dz} = a - yf$$
$$\frac{\partial v}{\partial z} = \frac{dv_0}{dz} + x\frac{d\theta_z}{dz} = b + xf$$
$$\frac{\partial w}{\partial z} = \frac{dw_0}{dz} - x\frac{d\theta_y}{dz} + y\frac{d\theta_x}{dz} = c - xd + ye$$

where *c*, *d*, *e*, *f* are constants along z-axis and displacements of each cross section can be obtained by the FEM calculation as described in the previous section.

The homogenized stiffness is then

$$< EA >= P / c$$
$$< EI_x >= M_x / e$$
$$< EI_y >= M_y / d$$
$$< GJ >= M_t / f$$

The calculated values are almost consistent for each cross section except near the two ends due to the boundary effects. The valid value can be chosen in the middle of the beam. Notice this method requires a FEM analysis for each cross section, and therefore it takes more than one hundred FEM runs to get the beam properties for a single rib.

2.4.3 Comparison of Different Beam Formulations

The two different beam formulations are compared. The line density is the same for all methods and is given in Figure 11 for the right 3rd rib of the Visible Man. Figure 12 to Figure 15 give the results for <EA>, <EIx>, <EIy>, and <GJ> respectively. It is clear from these figures that there exists only marginal difference in the calculated <EA>, <EIx>, and <EIy>. Classical beam formulation over-predicted torsion stiffness <GJ>. Since the torsion is only a very minor loading mode during high-speed impacts from KE-NLW and the computational cost of classical beam is significantly lower, the classical beam formulation is adopted.
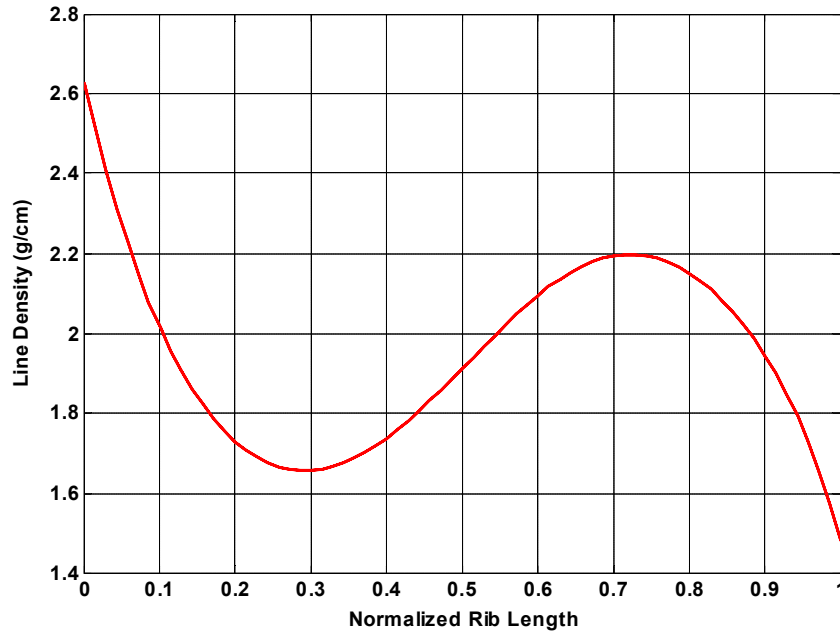
Figure 11. Line density as a function of rib length.
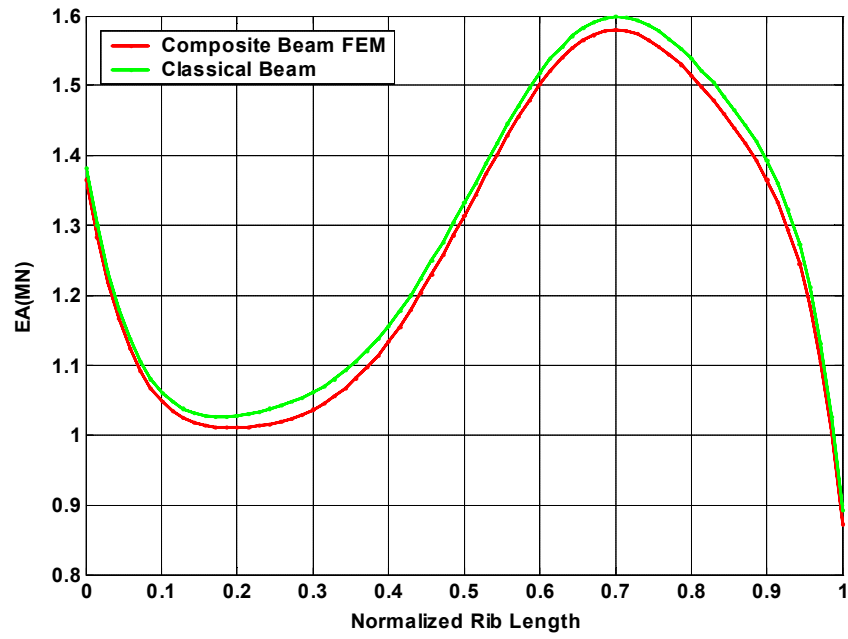
Figure 12. Homogenized tensile stiffness <EA> of the right 3rd rib of the Visible Man.
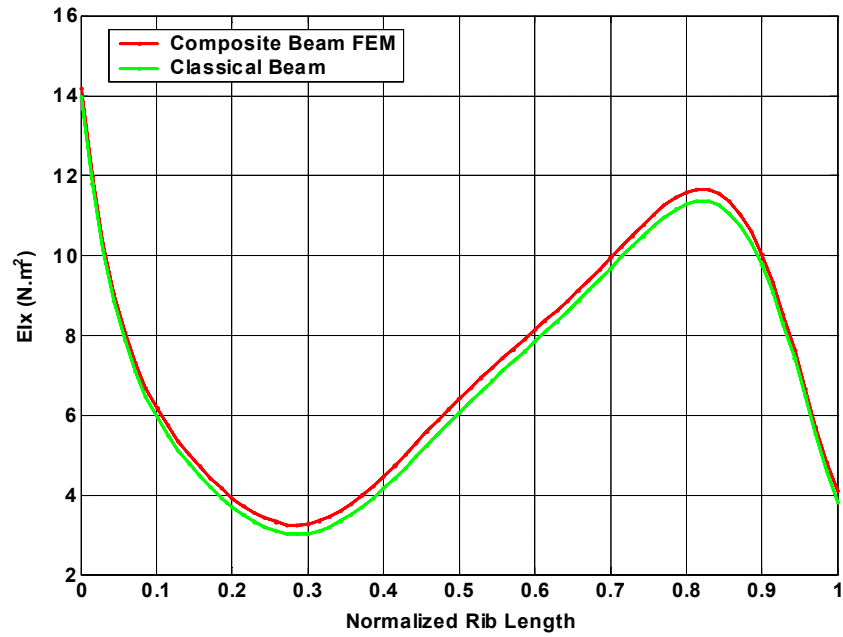
Figure 13. Homogenized flexural stiffness <EI$_x$> of the right 3rd rib of the Visible Man.
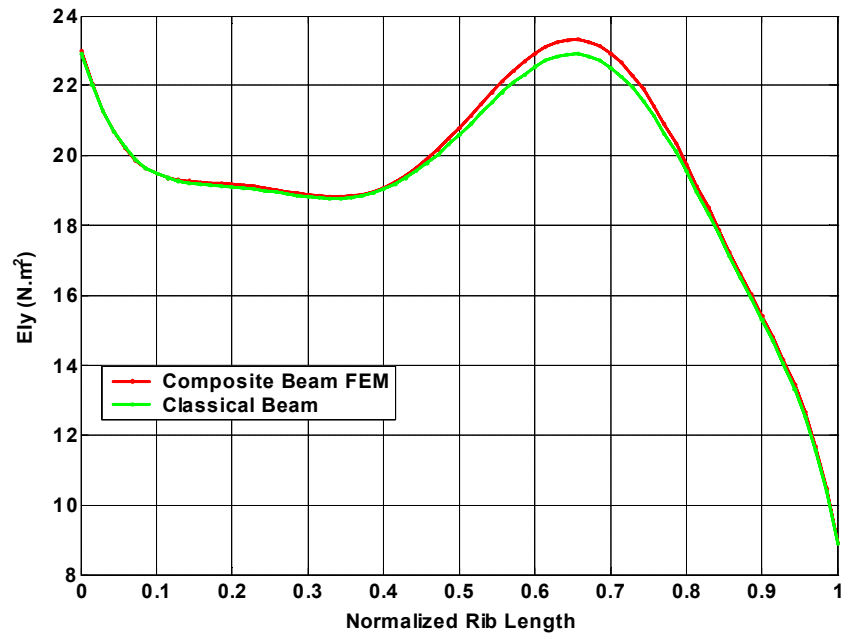
Figure 14. Homogenized flexural stiffness <EI$_y$> of the right 3rd rib of the Visible Man
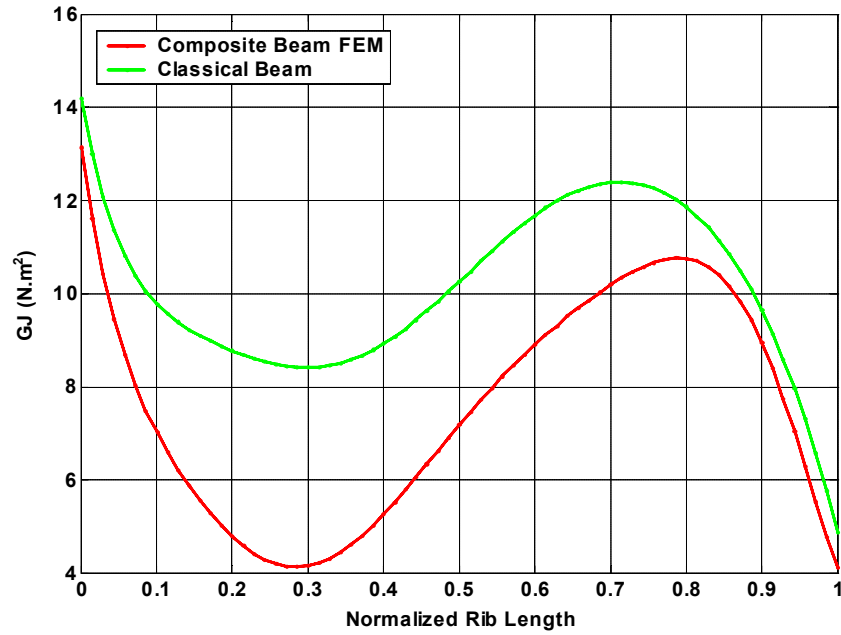
Figure 15. Homogenized torsion stiffness <GJ> of the right 3rd rib of the Visible Man.

2.5 Comparison of 3D FEM and Beam FEM of Ribs

A benchmark problem is set up and used to compare the calculated deformation, internal loads, and stresses from the 3D FEM and beam FEM. The benchmark problem, shown in Figure 16, is constructed from the right 3rd rib of the visible human and constrained on both ends of the rib in translations and is applied a half-sine impulse load over a certain cross section.

Figure 16. Illustration of the bench mark problem to compare 3D and beam FEM of rib.

Four meshes of different fineness as shown in Figure 17 are used for the 3D FEM. The element size in the finest mesh is smaller than the CT image pixel size, thus further refining the mesh will not improve the result of the 3D FEM.
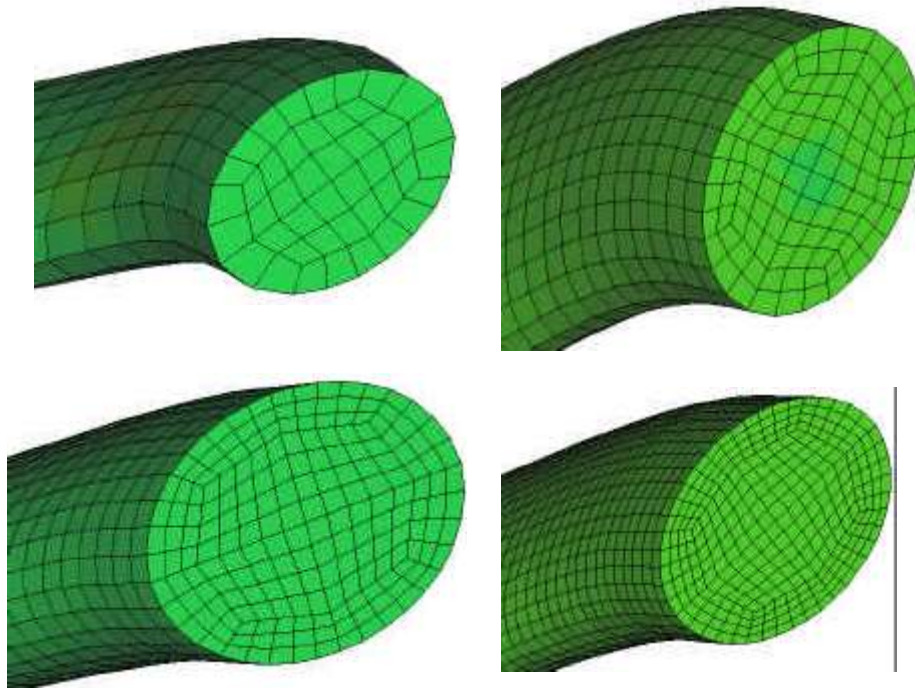
Figure 17. 3D FEM meshes used in the benchmark problem.

Figure 18 gives the calculated resultant displacements at the end of the impact load from the beam FEM and 3D FEM of four meshes. They can be interpreted as the "snapshots" of the displacements at that instant time. The deformations at both ends equal zero since the translations are constrained. With the increase of the mesh fineness of the 3D FEM, the calculated deformation, in terms of both peak value and the distribution along the rib, approaches the calculation of the beam FEM. The similar results are also shown in Figure 19, which gives the time history of deformation at the cross section that has the maximum deformation. Therefore, the beam formulation predicts deformation at least as good as the finest 3D FEM.
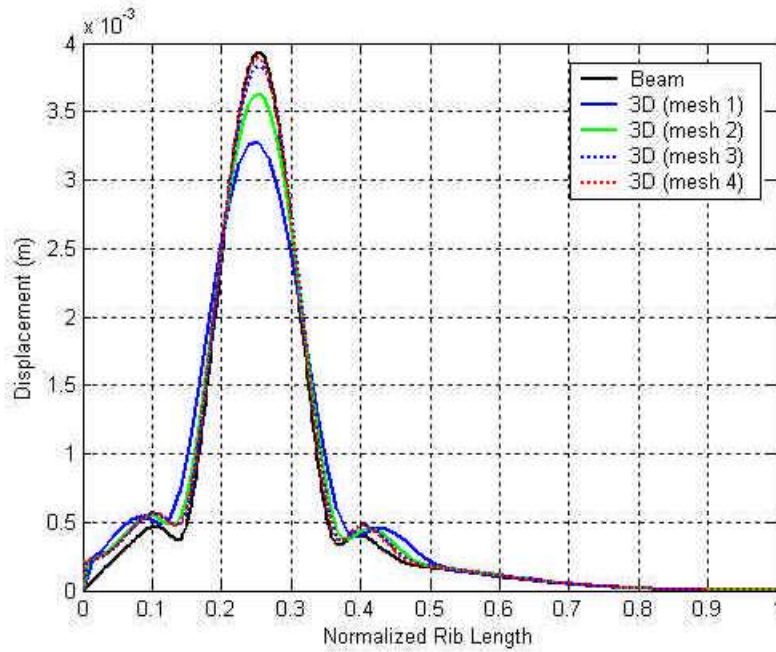
Figure 18. Displacement along the rib at the end of the impact load.

Figure 20 and Figure 21 give the similar "snapshot" and time history results of the bending moment along the short axis of the rib. Again, the 3D FEM calculations converge to beam FEM results with the increase of mesh fineness.
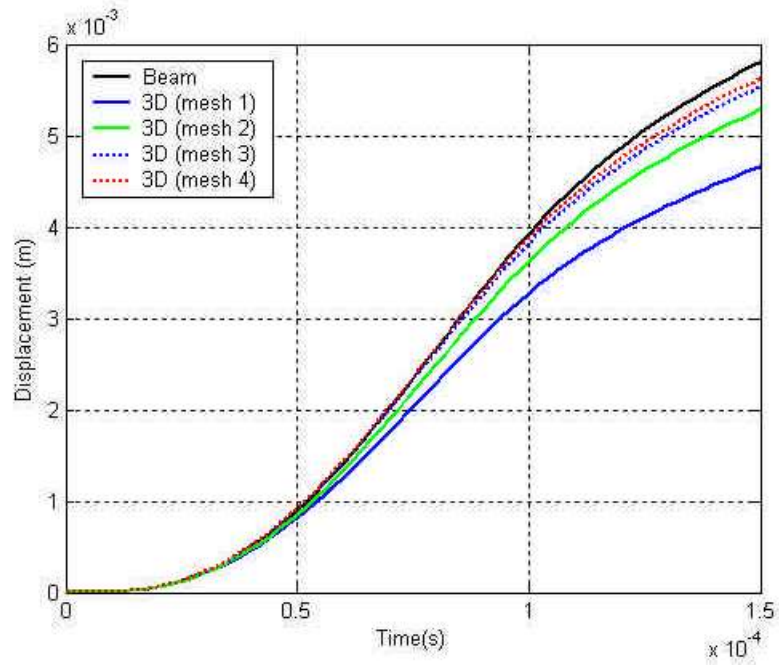
Figure 19. Displacement time history at the cross section with maximum deformation.
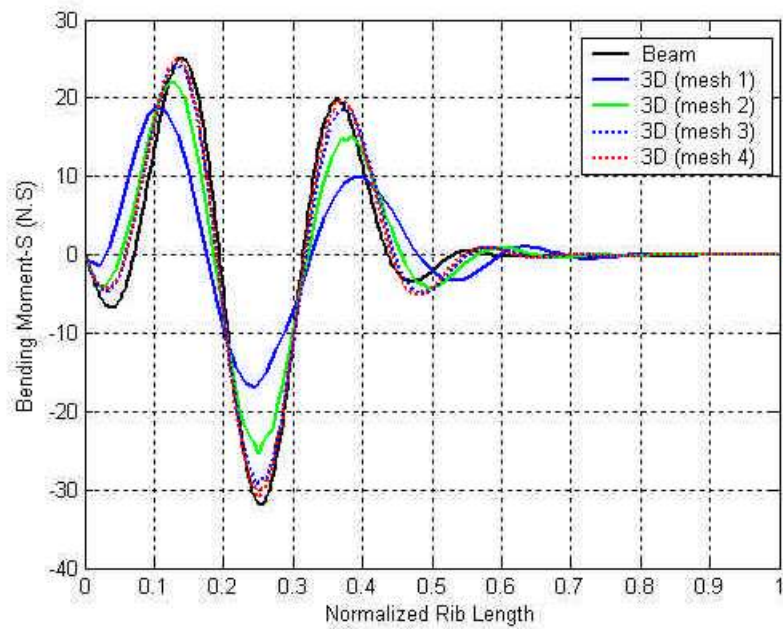
Figure 20. Bending moment along the short axis along the rib at the end of the impact.

18
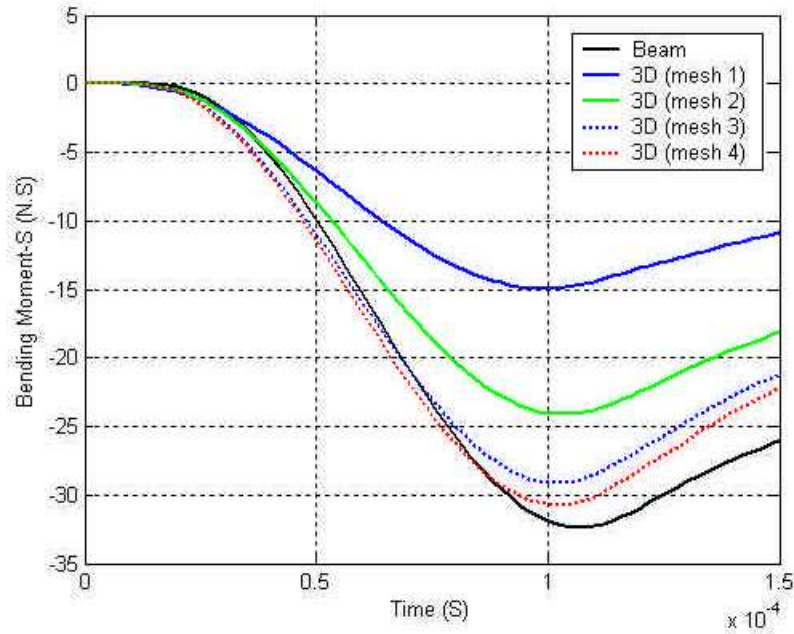
**Figure 21. The time history of bending moment along the short axis
at the cross section with maximum value.**

The similar results are also shown in Figure 22 and Figure 23, which give the similar "snapshot" and time history of the maximum tensile stress. It is also noticed that the 3D FEM with the coarsest mesh leads to errors in predicted peak stress of more than 100%. However, even this mesh has 44 elements in each rib cross section, which is much higher than most 3D rib meshes implemented in current thoracic finite element models (Deng *et al.* 2000; Chang 2001; Gordon R.Plank *et al.* 1998; Lizee *et al.* 1998). Therefore, it is questionable whether those models can accurately predict the rib fracture due to impact.

Table 1 shows the comparison of the computational cost of the beam FEM and 3D FEM. The CPU time is obtained running the benchmark problems on a Pentium IV 2.0 GHz dual processor PC using LS-Dyna3D finite element code. It is striking that the beam formulation runs 1000 times faster than the 3D FEM with the finest mesh, yet it yields better calculations of deformation, internal loads and stresses. Therefore the current beam formulation of rib is an efficient and accurate method of modeling ribs.
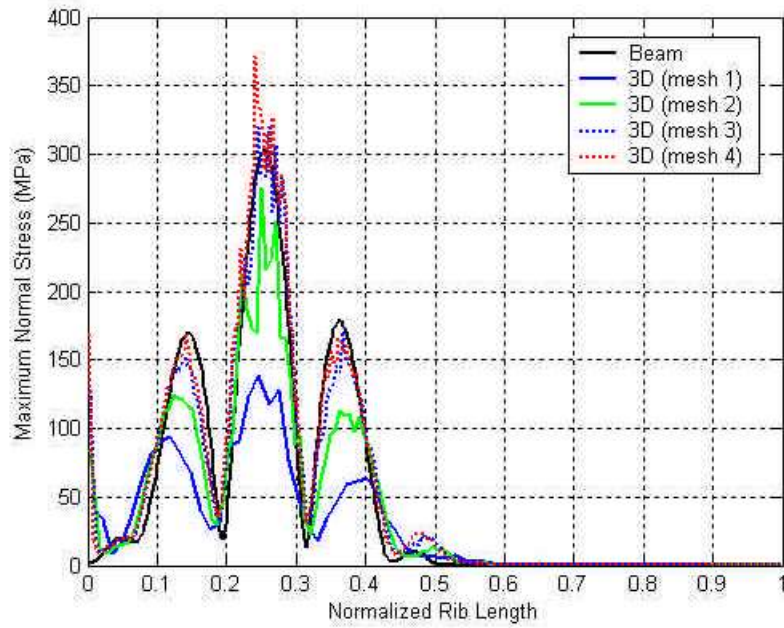
Figure 22. Maximum normal stress along the rib at the end of the impact.
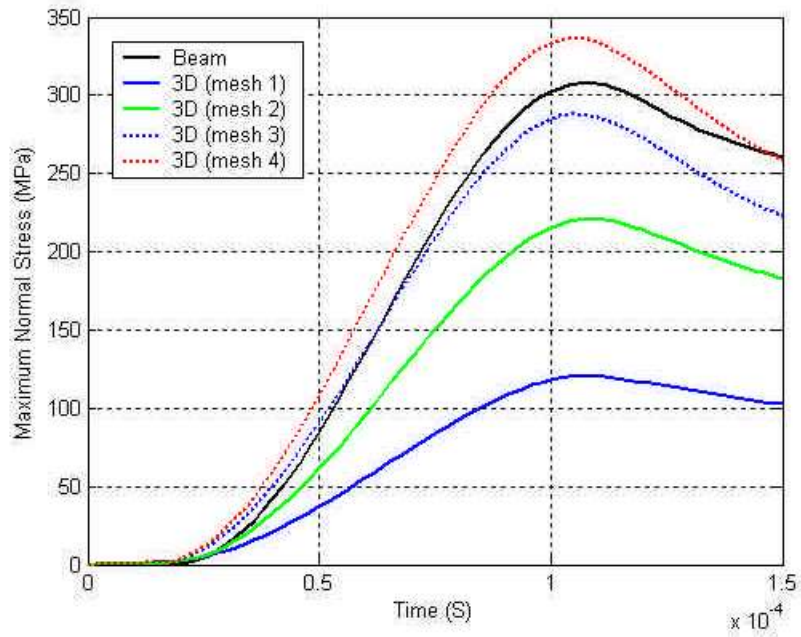
Figure 23. The time history of maximum normal stress at the cross section with maximum value.

Table 1. Comparison of computational cost of beam and 3D FEM of rib

	Nodes	Element	CPU Time
Beam FEM	570	284	9 sec
3D FEM (Mesh 1)	3970	3124	83 sec
3D FEM (Mesh 2)	17017	14768	13 minutes
3D FEM (Mesh 3)	44298	40044	1 hr 8 min
3D FEM (Mesh 4)	90915	84064	2 hr 52 min

3. Swine Thoracic FEM

3.1   Jaycor/UCSD Animal Test

Under a separate research project sponsored by the Army Medical Research and Materiel Command (MRMC), an animal study is ongoing to provide accurate anatomy and animal response data to controlled high-speed impacts. During an animal test, a full body CT scan is conducted for each individual animal subject under anesthesia to obtain high quality medical images. The animal is then subjected to a high-speed impact of an instrumented impactor. The sensor mounted on the impact records the acceleration during the impact. After the impact, a post-impact CT scan may be conducted and necropsy is performed to assess the injuries caused to the animal by the impact. Therefore, the animal study provides a detailed and accurate anatomy of the specific animal subject being tested, the response (motion, force) data of the animal during impact, and the injury data caused by the impact.

3.2   Subjective-specific Swine Thoracic FEM Based on Medical Imaging

A finite element model of swine thorax that is specific to the animal subject is then developed based on the medical imaging. The model involves a set of material parameters with baseline values determined from literature. It is calibrated by comparing the predicted and measured response data. The details of the swine thoracic FEM is given by Shen *et al.* 2003. A brief description of the model is given as follows.

Swine thoracic FEM is developed in two steps. The first step assembles the ribcage that includes ribs, spine and sternum. The second step creates FEM meshes for chest wall tissues and soft organs that include lungs, heart, diaphragm, skin, and chest-wall muscles. The treatment of the rib has been detailed in the previous chapter. Special treatment is also made to other components of the rib cage in order to reduce the computational cost. The spine is simplified using the model of Patwardhan *et al.* (1990) and Gilbertson (1993). The spine is represented by a series of linear beam elements, each representing a motion segment with nodes at the vertebral body centroids. Additional beam elements are added to transfer the forces and moments to the motion segments through the vertebral processes and the rib attachment points. The nodal coordinates are obtained from the CT images. The beam properties are obtained using the method in Gilbertson (1993). The sternum is reconstructed from the medical images to have the correct geometry, mass, and right contact with the chest wall, lungs and heart inside the chest cavity. The sternum is modeled as linear elastic 3D solid elements. The average density and Young's modulus estimated from CT images is assigned to the material. The costo-vertebral

joints are modeled as short beam with stiffness values from Closkey *et al.* (1992). The sterno-chondral joints are also modeled as short beam following the method used by Chen (1978) and Lee *et al.* (1995). Figure 24 shows the reconstructed geometry from the second animal test and the developed FEM for the rib cage of the pig.
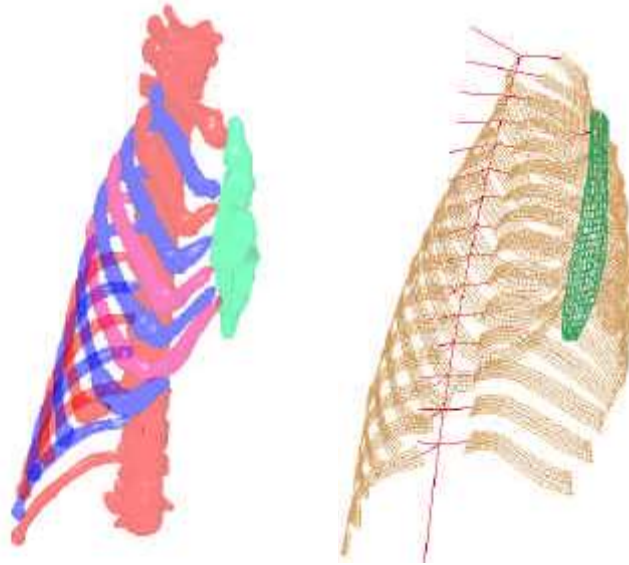
Figure 24. Constructed swine ribcage and FEM of the ribcage.

Geometries of the soft tissues and organs are also reconstructed from CT images. Lungs, heart, skin and skeletal muscles are modeled using 3D elements. Material constitutive relationships and parameters are based on literature and previous modeling work (Fung 1993; Yamada 1970; Dunn *et al.* 1983; Weiss *et al.* 1996; Truong *et al.* 1978; Truong 1974; Carter *et al.* 2001; Farshad *et al.* 1999; Liu *et al.* 2002; Liu *et al.* 2000; Miller 2000; Miller *et al.* 1997; Silver *et al.* 2001; Miller-Young *et al.* 2002; Deng *et al.* 2000). In general, soft tissues are modeled as nearly incompressible visco-hyperelastic materials. The nonlinear elasticity parameters are selected to best fit the available test data of tissue stress-strain relationships. Visco-elasticity is dealt with by using multiple terms of Prony series with the parameters determined to best match the available relaxation data and has a nearly constant hysteresis over the frequency ranges of interest. The constructed swine thoracic FEM for the animal subject is shown in Figure 25.
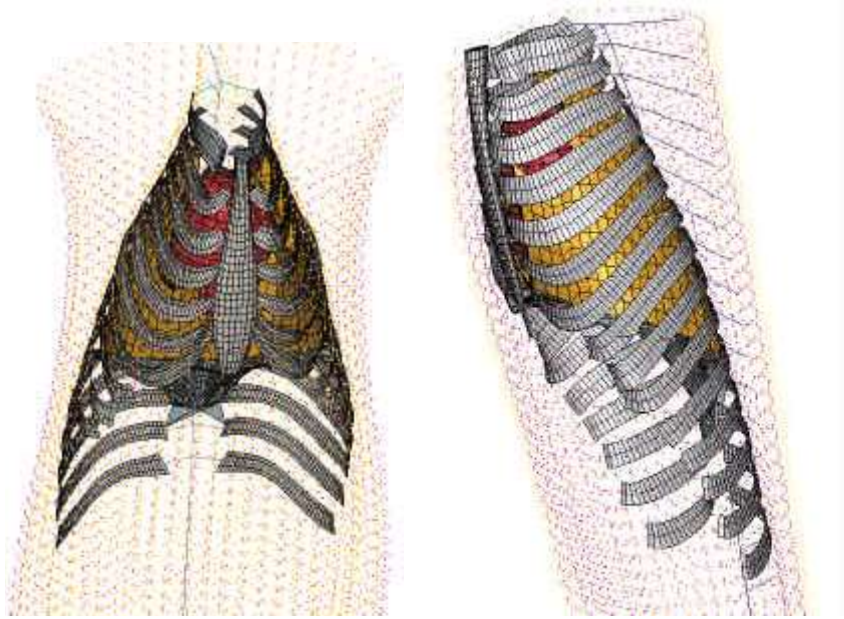
Figure 25. Swine thoracic FEM.

3.3   Validation of the Swine Thoracic FEM

Simulations of the animal tests (Figure 26) are conducted using the developed swine FEM. Impact force and chest wall deformation at the impact spot are compared with the experiment data. Using the baseline material parameters, determined as previously described, lead to good agreement of both the impact forces and impulses delivered to the animal chest for the two animal tests simulated. This validates the parameters used in the model.
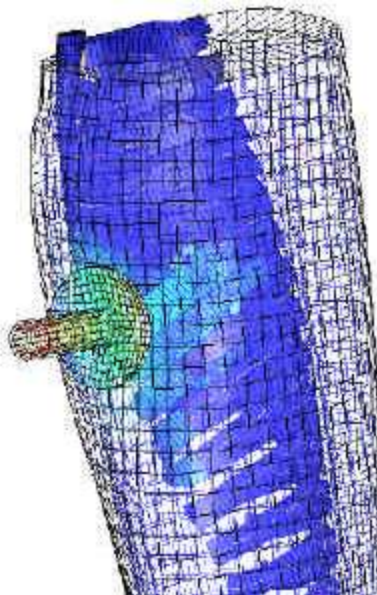
Figure 26. FEM simulation of an animal test.

4. Biomechanically-based Rib Fracture Correlation

4.1   Simulations of Animal Tests

The injury correlations for rib fracture were developed by relating the pathological data from animal studies to the response quantities calculated from the finite element simulation of the tests. Data from two animal studies were used. Two tests have been conducted in the Jaycor/UCSD animal study. The animal subjects, weighting 24 and 29 kg respectively, were impacted at 50 and 39 m/s by an instrumented impactor that was 7.62 cm in diameter and weighed 80 grams. The impacts were aimed between the 7th – 8th ribs on the right chest of the animal. In the first test, the 5th – 10th ribs were fractured along the anterior axillary line directly underneath the impact location. The second test broke the 8th rib of the animal. Finite element models were developed for each of the animals based on the CT images taken before the test. Model parameters were calibrated against the motion and impact history obtained from the accelerometers mounted on the impactors. The same set of parameters led to good agreement between FE estimation and measurements, indicating the validity of these FE models. Since the impact conditions in these tests were slightly different from the KE-NLW impacts, they help to validate the generality of the injury correlation developed.

In the WRAIR animal study, two types of NLW projectiles were used. There were 23 cases of steel ball impacts and 12 cases of sponge grenade impacts on the thorax. Most projectiles impacted the animal upper chest directly over the ribs with the exception of three tests where projectiles were aimed at the sternum. All rib impacts were assumed to be vertical to the ribs directly underneath the impact spot. Impact locations were determined from the test records and from the high-speed movie recordings of the impacts. Since medical images were not available. The finite element models were obtained by scaling the FEM developed for Jaycor/UCSD animal tests according to the weight of the subjects.
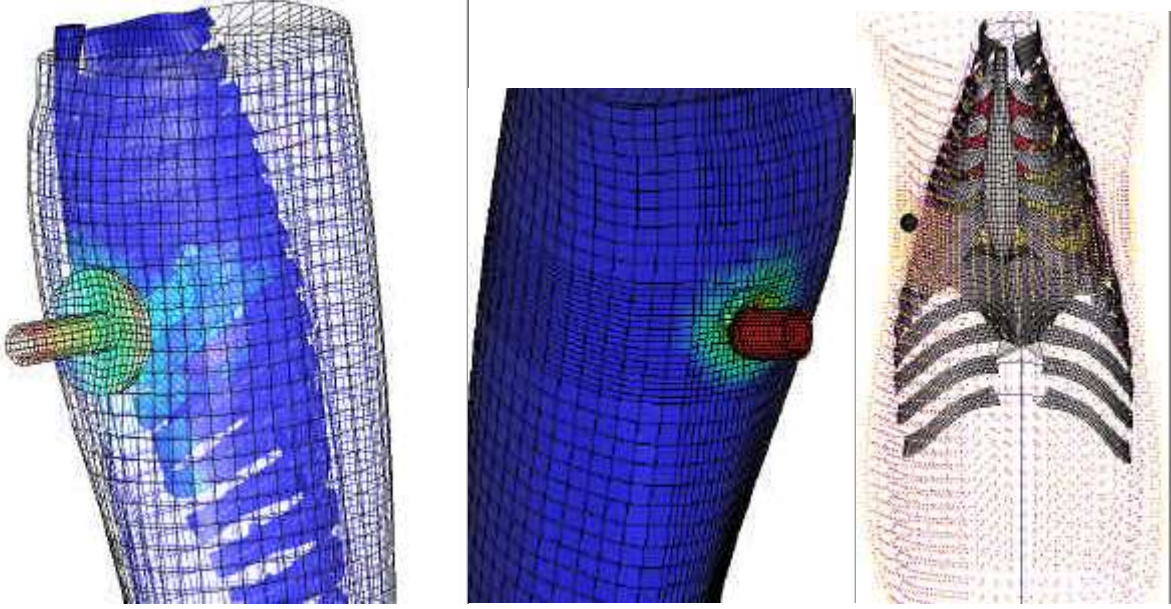
Figure 27. Simulations of animal studies.
(a) Jaycor/UCSD test; (b) WRAIR sponge grenade test; (c) WRAIR steel ball test

Figure 27 shows the FE simulation of the impactor, sponge grenade and steel ball impacts. FE models calculate the displacement and velocity time histories at each node and stresses and strains time histories in each element. For the purpose of establishing correlations, the maximum values an individual rib experienced during the impact were used as correlates. They represent the motion responses, internal forces, and stresses and strains of the ribs. Motion responses include displacement and velocity. Internal loads include bending moments, shear forces, tension, and torsion. The stress and strain-based failure criteria include those that have been used (Keyak *et al.* 2000) to predict the long bone failure as

Maximum principal stress: $S = \sigma_1$

Maximum shear stress: $S = (\sigma_1 - \sigma_3)/2$

Maximum normal strain: $E = \varepsilon_1$

Maximum shear strain: $E = (\varepsilon_1 - \varepsilon_3)/2$

Couloumb-Mohr failure theory: $(\sigma_1 / S_t) - (\sigma_3 / S_c) = 1$

Modified Couloumb-Mohr failure theory: $\begin{aligned} &S_t / \sigma_1 = 1 \text{ when } \sigma_1/\sigma_3 \leq -1 \\ &[(S_c - S_t)/ S_t S_c]\sigma_1 - (\sigma_3 / S_c) = 1 \text{ otherwise} \end{aligned}$

Hoffman stress: $\begin{aligned} &[1/(2S_t S_c)][(\sigma_1 - \sigma_2)^2 + (\sigma_2 - \sigma_3)^2 + (\sigma_3 - \sigma_1)^2] \\ &+ (1/ S_t - 1/ S_c)(\sigma_1 + \sigma_2 + \sigma_3) = 1 \end{aligned}$

28

Distortion energy: $S = \sqrt{\dfrac{1}{2}[(\sigma_1 - \sigma_2)^2 + (\sigma_2 - \sigma_3)^2 + (\sigma_3 - \sigma_1)^2]}$

where $\sigma_1, \sigma_2, \sigma_3$ and $\varepsilon_1, \varepsilon_2, \varepsilon_3$ are the principal stresses and strains, S_t, S_t are the tensile and compressive strengths, and E is the ultimate strain, respectively.

4.2   Finite Element Simulation Results

For two Jaycor/UCSD tests, the calculated values of the maximum failure criteria of each rib are given in Table 2. The values corresponding to fractured ribs are shared in the table. Similar results are also given in Table 3 for one WRAIR test where the 6th rib was fractured under the impact of a rubber covered steel ball at 64.1 m/s and in Table 4 for another test where the 6th and 7th ribs were fractured by a sponge grenade impact at 89.1 m/s. In all the cases, the location of maximum stresses or strains matched very well with the actual fracture spots. It is also clear that the fractured ribs tend to have large values than those not fractured. Threshold values for fracture appear consistent. For example, the threshold principal stress is between 108.55-155.45 MPa from the second Jaycor/UCSD test, about lower than 143.17 for the WRAIR steel ball test, and about lower than 145.94 or 129.88 for the WRAIR sponge grenade test. Similar results are observed for other stress or strain-based criteria. The values for ribs that were not first fractured in the first Jaycor/UCSD were not used in statistical analysis since their the values (except for the first fracture rib) may be underestimated since the post-failure response was not included in the model.

Table 2. FEM Calculation of the Jaycor/UCSD Animal Studies

Rib #	Normal Stress (Mpa)	Shear Stress (Mpa)	Normal Strain (%)	Shear Strain (%)	Coulomb Mohr (MPa)	Modified Mohr (MPa)	Hoffman Value (MPa)	Distortion Energy (MPa)
			First test					
R02	36.0	41.7	0.4	0.6	37.1	36.0	36.5	41.1
R03	41.3	45.5	0.4	0.7	42.1	41.3	41.6	45.0
R04	54.6	59.8	0.5	0.8	54.9	54.6	54.7	59.6
R05*	103.5	116.8	0.9	1.5	103.9	103.5	103.7	116.6
R06†	182.3	197.5	2.3	3.1	183.2	182.3	182.6	196.9
R07*	117.8	118.8	1.6	2.1	118.6	117.8	118.1	118.3
R08*	75.7	77.4	1.2	1.6	77.1	75.7	76.3	76.6
R09*	67.4	71.5	1.1	1.8	67.8	67.4	67.6	71.3
R10*	94.0	101.3	0.9	1.4	94.4	94.0	94.2	101.1
R11	29.1	34.7	0.4	0.7	33.5	29.1	31.3	32.2
R12	17.7	21.6	0.3	0.5	20.1	17.7	18.5	19.6
R13	14.5	21.1	0.2	0.5	19.6	14.5	17.2	18.5
R14	16.3	22.9	0.3	0.5	21.3	16.3	18.9	20.4
			Second test					
R02	6.77	7.97	0.10	0.15	7.12	6.77	6.93	7.50
R03	9.27	11.38	0.15	0.25	10.13	9.27	9.61	10.79
R04	11.19	12.24	0.14	0.22	11.99	11.19	11.49	11.67
R05	18.63	20.76	0.22	0.34	19.42	18.63	18.98	20.30
R06	40.47	45.09	0.37	0.56	40.92	40.47	40.66	44.83
R07	70.08	75.62	0.73	1.15	70.47	70.08	70.24	75.35
R08	155.45	156.40	2.13	2.86	156.21	155.45	155.77	155.92
R09	108.55	122.79	1.17	1.66	108.69	108.55	108.61	122.71
R10	94.80	95.18	1.03	1.41	95.11	94.80	94.93	94.99
R11	35.75	38.00	0.38	0.59	37.34	35.75	36.37	36.67
R12	23.56	24.08	0.20	0.32	23.98	23.56	23.74	23.83
R13	19.53	25.49	0.25	0.46	23.05	19.53	21.30	23.74
R14	20.30	27.12	0.29	0.53	25.76	20.30	23.24	24.44

†: The rib that was first fractured according to FEM simulation

*: These ribs were not included in the statistical analysis since these values were underestimated because post-failure response of ribs was not included in the FEM

Table 3. FEM Calculation of on WRAIR Steel Ball Test

Rib #	Principle Stress (Mpa)	Shear Stress (Mpa)	Normal Strain (%)	Shear Strain (%)	Coulomb Mohr (MPa)	Modified Mohr (MPa)	Hoffman Value (MPa)	Distortion Energy (MPa)
R02	10.09	14.03	0.18	0.32	11.62	10.95	11.11	13.81
R03	17.03	18.49	0.23	0.35	18.20	17.03	17.56	17.80
R04	32.30	32.56	0.31	0.46	32.51	32.30	32.39	32.43
R05	65.98	66.35	0.62	0.94	66.27	65.98	66.10	66.16
R06	143.17	143.34	1.28	1.75	143.31	143.17	143.23	143.26
R07	43.85	58.25	0.46	0.69	46.63	46.51	46.56	58.18
R08	26.56	28.60	0.47	0.70	27.92	26.56	27.00	27.64
R09	28.04	43.77	0.77	1.44	40.12	28.04	35.23	38.63
R10	23.52	27.31	0.31	0.54	26.55	23.52	24.97	25.62
R11	15.28	22.45	0.30	0.56	20.87	15.28	18.49	19.93
R12	10.13	14.25	0.18	0.33	13.43	10.13	11.98	12.70
R13	8.82	13.24	0.17	0.32	12.27	8.82	10.81	11.73
R14	9.48	14.13	0.19	0.36	13.20	9.48	11.65	12.47

Table 4. FEM Calculation of on WRAIR Sponge Grenade Test

Rib #	Principle Stress (Mpa)	Shear Stress (Mpa)	Normal Strain (%)	Shear Strain (%)	Coulomb Mohr (MPa)	Modified Mohr (MPa)	Hoffman Value (MPa)	Distortion Energy (MPa)
R02	14.73	21.83	0.28	0.51	20.41	14.73	18.03	19.28
R03	15.35	23.10	0.35	0.64	21.55	15.35	18.99	20.36
R04	21.51	23.03	0.32	0.47	22.73	21.51	22.06	22.31
R05	40.02	46.72	0.36	0.57	40.25	40.02	40.12	46.60
R06	129.88	137.96	1.23	1.77	130.82	129.88	130.28	137.41
R07	145.94	149.81	1.30	1.95	146.30	145.94	146.09	149.58
R08	60.80	65.12	0.91	1.41	61.70	60.80	61.18	64.84
R09	49.42	77.31	1.46	2.73	71.73	49.42	62.85	67.81
R10	27.43	33.75	0.47	0.76	30.67	27.43	28.81	31.45
R11	22.31	35.02	0.52	0.97	32.47	22.31	28.43	30.70
R12	15.86	24.09	0.31	0.58	22.44	15.86	19.75	21.21
R13	26.60	41.26	0.48	0.89	38.25	26.60	33.56	36.26
R14	23.18	34.84	0.44	0.81	32.50	23.18	28.65	30.71

4.3　Statistical Analysis

Statistical analysis was conducted using the animal test injury data and the FEM calculation of motion responses, internal forces, and stress and strain-based failure criteria. The analysis was performed in two steps. First, statistics of the regressions for three different impact conditions were analyzed separately to determine significant correlates that better fit the data under different impact conditions. Second the regression curves of the selected correlates under three impact conditions were plotted together. Regression curves of a good correlate have to agree with each other.

The dependent variable, rib fracture, was assigned YES (1) if a specific rib was fractured during a test or NO (0) otherwise. Numbers 1, 2, and 3 were assigned for three projectiles: steel

ball, sponge grenade, and the Jaycor/UCSD instrumented impactor respectively. Numbers 1 and 2 also indicated two impact locations, chest and sternum, respectively. The variables included motion responses, internal forces, and stress and strain-based failure criteria.

Since the data was discrete, binomial, and not heteroskedastic, the logistic regression model was used to estimate the factors that influence rib factures. The regression function is expressed as

$$P = \frac{1}{1 + \exp(-\alpha - \beta x)}$$

where P is the probability of rib fracture (dependent variable), (interceptor) and (slope) are the best-fit model parameters determined from maximum likelihood estimation, and X the independent variable used for the regression. Data for three projectiles were analyzed separately.

Six ribs were fractured in the first Jaycor/UCSD animal test. The 6th rib was fractured first with ribs 5 and 7 to 10 following. This led to the underestimation of peak stresses and strains in ribs 5 and 7 to 10 since previous fractured ribs would have lost some load-carrying capability, which was not considered in the FEM. Therefore, the ribs 5 and 6–10 were not used in the analysis. The Jaycor/UCSD data set thus has 21 samples (8 ribs for the first test and 13 ribs for the second test) with 19 nonfractured ribs and 2 fractured ribs.

Table 5 gives the results of the logistic regression of the Jaycor/UCSD tests. The statistics listed include deviance, χ^2 value, MacFadden's R^2 values, and percentage of correct prediction of the sample. A star after a χ^2 value indicates that the variable is statistically significant at 0.001 level (99.9% confidence level). Larger χ^2 values indicate that the variable is more statistically significant. Smaller deviance and larger MacFadden's R^2 values indicate that the variable fits better to the data. Since the data set contains a significant number of nonfractured ribs that are usually associated with very small values, the percentage of correction predicted values are very high. It should only be taken in the relative sense.

For this specific data set, significant correlates include the peak rib velocity, bending momentum along the long axis, shear force along the short axis, and all stress and strain-based variables. All stress and strain-based correlates perfectly fit the data. However, it has to be noted that this is a very small data set that includes only two injury data points. All stress-based variables in general are better correlates that have smaller deviations and higher R^2 values, compared with the motion and internal force variables. Strains, however, do not fit the data as well as stress-based variables and have much higher deviation.

Table 5. Results of Logistic Regression (Jaycor/UCSD)

Criteria	•	β	Deviance	χ^2	McFadden's R^2	% Correct Prediction
Motion						
Rib Displacement	-6.120	11.0485	2.23	0.14	83	83.130
Rib Velocity	-8.834	0.5556	0.04	13.17*	100	1.000
Internal Force						
Moment in long axis	-6.421	0.5016	0.19	13.02*	99	1.000
Moment in short axis	-6.762	0.8407	2.59	10.62	80	0.952
Shear in long axis	-3.510	0.0022	6.91	6.30	48	0.952
Shear in short axis	-8.341	0.0056	0.16	13.05*	99	1.000
Tension	-20.406	0.0235	0.28	12.93*	98	1.000
Torsion	-12.009	1.2680	0.00	13.21*	100	1.000
Stress and Strain						
Principal Stress	-13.555	0.1033	0.00	13.21*	100	1.000
Shear Stress	-14.007	0.1010	0.00	13.21*	100	1.000
Normal Strain	-12.436	7.5893	0.00	13.21*	100	1.000
Shear Strain	-12.569	5.5996	0.00	13.21*	100	1.000
Couloumb-Mohr Stress	-13.507	0.1026	0.00	13.21*	100	1.000
Modified Couloumb-Mohr	-13.555	0.1033	0.00	13.21*	100	1.000
Hoffman Stress	-13.537	0.1030	0.00	13.21*	100	1.000
Distortion Energy	-14.028	0.1014	0.00	13.21*	100	1.000

Table 6 and Table 7 give the results of the logistic regress of WRAIR test using steel balls and sponge grenades respectively. The steel ball data set includes 23 tests (299 rib samples), among which 8 subjects suffered a single rib fracture. The sponge grenade data has 12 tests (156 samples) with 4 subjects had two fracture ribs.

The χ^2 statistics for steel ball and sponge grenade data sets indicate that peak rib deformation is not a significant correlate of rib fracture. This agrees with the analysis of the Jaycor/UCSD data. This is in stark contrast to car crash impacts where chest deformation is generally accepted as a good indicator of rib fracture.

The bending moment along the long axis and shear force along the short axis are significant correlates for all three impact conditions. This result was expected since the impact directions were primarily along the short axis (vertical to the exterior of the rib cage), therefore the shearing along the impact direction and the local bending along the long axis should be the primary loading modes. The tension becomes significant in sponge grenade impacts. Both tension and torsion are significant in the Jaycor/UCSD tests. The diameters of the projects are about 1.8 cm for a steel ball (covering one rib), 4 cm for a sponge grenade (covering two ribs), and 7.5 cm for the Jaycor/UCSD impactor (covering two and more ribs). This suggests that with

the increase of projectile diameter, which tends to involve more global response of the ribcage, extra loading modes such as tension and torsion become more important.

Table 6. Results of Logistic Regression (Steel ball)

Criteria	•	β	Deviance	χ^2	McFadden's R^2	% Correct Prediction
Motion						
Rib Displacement	-4.520	16.2966	30.69	0.00	58	0.967
Rib Velocity	-4.964	0.4387	27.33	46.39*	63	0.977
Internal Force						
Moment in long axis	-3.061	0.0806	47.52	26.20*	36	0.967
Moment in short axis	-2.351	0.0466	69.00	4.73	6	0.973
Shear in long axis	-1.293	-0.0005	69.18	4.54	6	0.973
Shear in short axis	-3.260	0.0012	54.50	19.22*	26	0.967
Tension	-2.491	0.0009	64.12	9.60	13	0.973
Torsion	-2.217	0.0528	69.83	3.89	5	0.973
Stress and Strain						
Principal Stress	-6.747	0.0518	18.14	55.58*	75	0.983
Shear Stress	-7.365	0.0558	17.36	56.36*	76	0.983
Normal Strain	-6.812	5.5735	23.96	49.76*	68	0.980
Shear Strain	-4.749	2.3506	37.52	36.20*	49	0.973
Couloumb-Mohr Stress	-6.768	0.0519	18.21	55.51*	75	0.983
Modified Couloumb-Mohr	-6.772	0.0520	18.10	55.62*	75	0.983
Hoffman Stress	-6.765	0.0519	18.15	55.57*	75	0.983
Distortion Energy	-7.321	0.0555	17.37	56.35*	76	0.983

Table 7. Results of Logistic Regression (Sponge Grenade)

Criteria	•	β	Deviance	χ^2	McFadden's R^2	% Correct Prediction
Motion						
Rib Displacement	-2.193	2.5205	55.78	0.00	12	0.942
Rib Velocity	-4.104	0.3581	28.49	34.62*	55	0.962
Internal Force						
Moment in long axis	-3.125	0.0789	34.17	28.94*	46	0.955
Moment in short axis	-2.248	0.0489	55.08	8.03	13	0.942
Shear in long axis	-1.617	0.0000	63.10	0.01	0	0.949
Shear in short axis	-3.106	0.0012	39.42	23.69*	38	0.949
Tension	-2.688	0.0010	42.40	20.71*	33	0.942
Torsion	-2.100	0.0557	56.67	6.44	10	0.936
Stress and Strain						
Principal Stress	-5.968	0.0441	19.27	43.84*	69	0.968
Shear Stress	-4.925	0.0333	20.71	42.40*	67	0.962
Normal Strain	-4.296	3.1622	27.17	35.94*	57	0.949
Shear Strain	-3.963	1.8477	29.65	33.46*	53	0.955
Couloumb-Mohr Stress	-6.095	0.0449	19.23	43.88*	70	0.968
Modified Couloumb-Mohr	-5.968	0.0441	19.27	43.84*	69	0.968
Hoffman Stress	-6.018	0.0444	19.25	43.86*	69	0.968
Distortion Energy	-4.865	0.0329	20.73	42.38*	67	0.962

In agreement with the Jaycor/UCSD result, stress-based variables fit the sponge grenade and steel ball data much better (smaller deviation, larger R^2 value) than the motion responses and internal forces. Among motion and internal force variables, peak velocity, bending moment along the long axis, and shear force along the short axis fit relatively better than the others. Strains are not as good correlates as stresses but are generally better than motion and internal force variables. There is no significant difference among different stress-based variables.

Based on these results, the following variables were selected for further analysis: peak velocity, bending moment along the long axis, shear force along the short axis, and all stress and strain-based variables.

A good correlate should be valid over a variety of impact conditions, therefore, similar regression curves should be obtained for the Jaycor/UCSD tests, WRAIR sponge grenade tests and WRAIR steel ball tests. Figure 28 gives the correlation between the stresses, including normal and shear stresses, and the probability of rib fracture for the three impact conditions. The three thick lines, dotted, dashed, and solid lines, are the logistic regression curves based on the Jaycor/UCSD test data, WRAIR sponge grenade test data, and WRAIR steel ball test data respectively. The corresponding thin lines indicate the 95% confidence bands of the regression.

The normal stresses for 50% injury are very close, about 130, 131.5, and 135 MPa respectively for the three cases. Furthermore, the three regression curves all fall into the confidence bands of each other within the range where the data are meaningful. For shear stress, the 50% values are also very close, about 132, 138 and 147 MPa respectively. Also the regression curves are within the confidence bands of other data sets. Similar results are also obtained for all the other stress-based criteria.
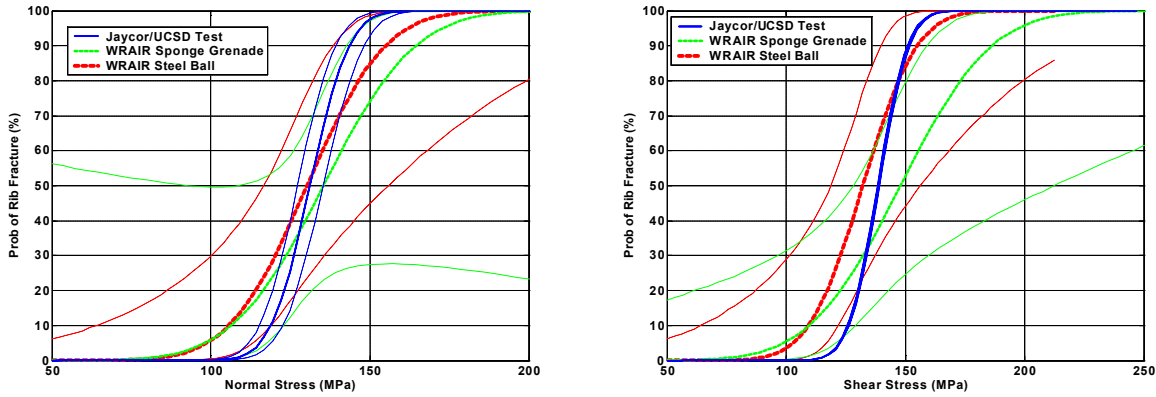

Figure 28. Correlation of stresses versus probability of rib fracture.

Figure 29 gives the regression curves using strains as correlates. The 50% values for normal strain are 1.63%, 1.2%, and 1.35% respectively for the Jaycor/UCSD test, sponge grenade impacts and steel ball impacts. The variation is much larger than that using stresses as correlates and the regression curves of the Jaycor/UCSD test falls significantly out of the confidence bands of regression curves of the other cases. The results are slightly better for shear strain. This reaffirms the conclusion that strains do not fit the data set as well as stress variables.
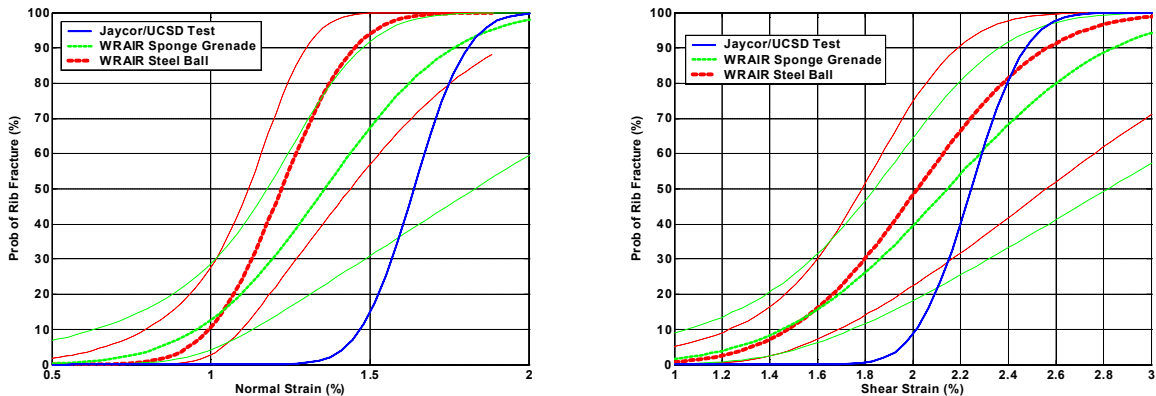

Figure 29. Correlation of strains versus probability of rib fracture.

36

Figure 30 gives the regression curves using peak rib velocity and bending moment along the long axis as correlates. The correlations are clearly inconsistent. Although the regression curves for the sponge grenade and steel ball data match well with each other, they are significantly different from the Jaycor/UCSD tests where impact velocities were slightly lower and impactors were slightly heavier.
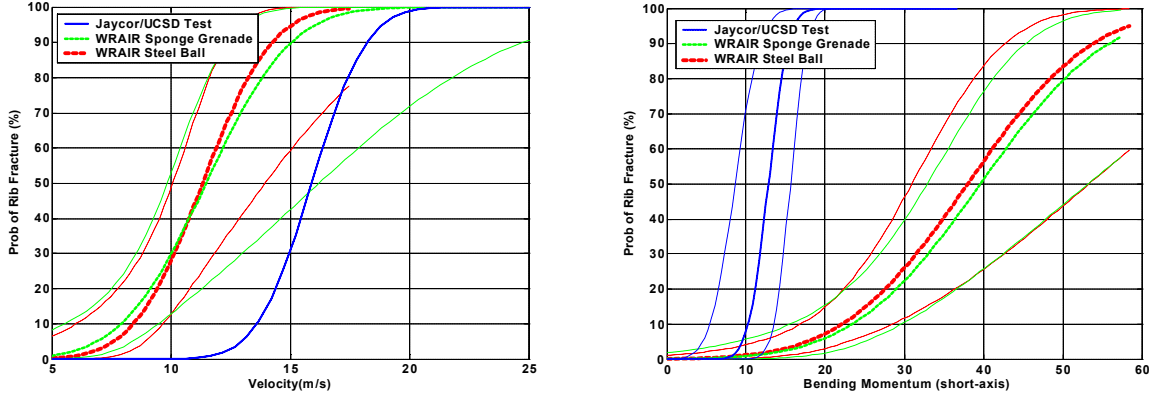
Figure 30. Correlation of velocity and bending moment versus probability of rib fracture.

4.4 Rib Fracture Correlations for KE-NLW Impacts

The statistical analysis shows that stress-based failure criteria are the best correlates of rib fracture. There is no clear difference among the stress variables studied. Therefore, the stress-based rib fracture correlations are obtained from the logistic regression using the data set combing all the cases. Table 8 gives the statistics of the regression, indicating that they are all good correlates based on the data. The values for strains are also provided only for the purpose of comparing them against available bone strength data. It is not recommended that they be used as correlates of rib fracture. The regression curves and the confidence bands of the regressions are given in Figure 31 for normal stress and shear stress.

Table 8. Statistics of rib fracture correlation

| Criteria	•	β	Deviance	χ^2	Wald-χ^2	McFadden's R^2	% Correct Prediction
Principal Stress	-6.826	0.0515	38.22	114.99	13.53	75.060	0.977
Shear Stress	-6.036	0.0432	41.19	112.02	18.25	73.120	0.975
Couloumb-Mohr Stress	-6.856	0.0516	38.23	114.98	13.91	75.050	0.977
Modified Couloumb-Mohr	-6.844	0.0517	38.18	115.03	13.53	75.080	0.977
Hoffman Stress	-6.845	0.0516	38.21	115.01	13.73	75.060	0.977
Distortion Energy	-5.991	0.0429	41.21	112.01	18.06	73.1	0.975
Normal Strain	-5.419	4.1911	53.88	99.33	23.77	64.830	0.973
Shear Strain	-4.412	2.1149	68.4	84.81	31.61	55.350	0.968
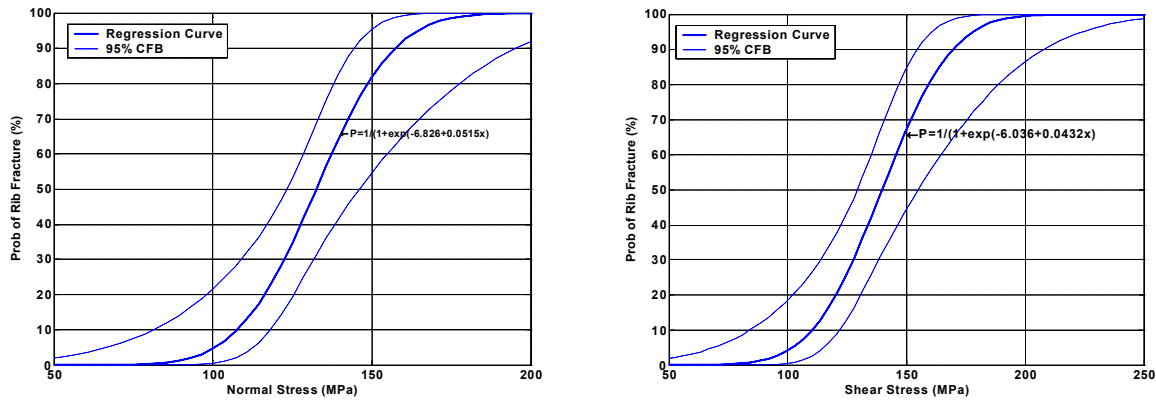
Figure 31. Rib fracture correlation curve based on normal and shear stresses.

These values are consistent with the values reported in literature under different loading conditions. Kaneko *et al.* (2003) reported the mean values of ultimate normal stress to be between 91.7 – 110.8 and 91.7 – 161.3 MPa from laboratory tests of cortical bones under tension and compression respectively. Currey (1990) gave the values in range of 100 – 200 MPa for long bones of many species. Reilly *et al.* (1975) gave the overall values of ultimate stresses for human bone as 133 (tension, longitudinal direction), 193 (compression, longitudinal direction), 68 (tension, transverse direction), and 133 (compression, transverse direction). Taylor *et al.* (2002) also gave the value between 60 to140 determined from fatigue tests. The regression developed gives the 50% normal stress value of 127.5 MPa, with the 95% confidence range being 127 – 138 MPa. They compare very well against the bone strength data from the literature, which were obtained from very different loading conditions. This suggests that the stress-based correlations address the right mechanism of the rib fracture. They may be general enough to be used beyond the high-speed blunt impact conditions from which they are developed.

5. Summary

Previous animal study data and actual human injury data from the application of NLW indicated that rib fracture is a common type of injury that can be caused by the high-speed blunt impact of NLW projectiles. Rib fracture can lead to severe injury or even lethality. There have been not correlates specifically developed for rib fractures under these high-speed impact conditions. Analysis of correlates developed for lower-speed car crash impacts showed that those correlations did not work under NLW impact conditions.

Based on an ongoing animal study conducted jointly by Jaycor and UCSD, another animal study conducted by WRAIR, and the ongoing work of developing subject-specific FEM of animal and human subjects, this study developed a biomechanically-based rib fracture criteria for high-speed impact.

First, a detailed finite element model (FEM) of ribs was developed. This rib FEM was based on geometry constructed from high-resolution CT images. CT numbers were used to determine the density and elastic modulus of each pixel. Different material parameters were assigned to a corresponding element, therefore, this was a detailed 3D inhomogeneous FEM. To reduce the computational cost, several beam formulations were developed to convert the complex inhomogeneous rib structure into equivalent beam models that respond the same under the impacts. Each beam node was assigned material parameters determined from the material distribution in the rib cross section it represented, therefore, the beam FEM was also inhomogeneous. Extensive numerical study was conducted and it was concluded that the beam FEM was far more efficient numerically and was at least as accurate as a very finely meshed 3D rib FEM. The rib FEM was then implemented into the subject-specific swine thoracic FEM models that were also constructed from CT images. After being calibrated against the response measurements from the Jaycor/UCSD tests, the finite element models were used to simulate the Jaycor/UCSD tests and the WRAIR animal tests using both sponge grenades and steel balls. Model calculations of the peak motion responses, internal forces, and a number of stress and strain-based quantities for each rib were correlated to rib fracture potential using logistical regression. Statistical analysis indicates that the stress-based criteria correlate much better to the data than the motion responses and internal forces. This conclusion is intuitive since a fundamental mechanism of rib fracture is that the stress exceeds the strength of the rib bone. There is no significant difference among various stress-based variables. However, strains are not as good correlates as stresses. In addition, in contrast to car crash impacts where chest deformation is

believed to be a good correlate, peak rib deformation is not a good correlate under high-speed, lower-mass impact conditions.

Correlation curves using stresses as correlates were developed and are provided in the report. The correlations fitted the animal test data very well and the threshold values are consistent with bone strength data found in the literature. The FEM modeling of rib can be easily incorporated into a human thoracic FEM to predict bone stresses under impact. And since the injury correlations represent the fundamental relationship between bone stress and strength, it is believed to be valid for humans.

6. References

Ackerman, M. J. The Visible Human Project. J.Biocommun. 18[2], 14. 91.

Bir, Cynthia Ann. The evaluation of blunt ballistic impacts of the thorax. 164. 00. WAYNE STATE UNIVERSITY.

Carter, D. R. and Hayes, W. C. Compact bone fatigue damage: a microscopic examination. Clin.Orthop. [127], 265-274. 77.

Carter, F. J., Frank, T. G., Davies, P. J., McLean, D., and Cuschieri, A. Measurements and modelling of the compliance of human and porcine organs. Med.Image Anal. 5[4], 231-236. 01.

Chang, H. S. The development, validation, and comparison of a finite element human thorax model for automotive injury. 01.

Chen, P. H. Finite element dynamic structural model of the human thorax for chest impact response and injury studies. Aviat Space Environ Med 49[1 Pt. 2], 143-9. 78.

Choi, K. and Goldstein, S. A. A comparison of the fatigue behavior of human trabecular and cortical bone tissue. J.Biomech. 25[12], 1371-1381. 92.

Closkey, R. F., Schultz, A. B., and Luchies, C. W. A model for studies of the deformable rib cage. J.Biomech. 25[5], 529-539. 92.

Couteau, B., Hobatho, M. C., Darmana, R., Brignola, J. C., and Arlaud, J. Y. Finite element modelling of the vibrational behaviour of the human femur using CT-based individualized geometrical and material properties. J Biomech 31[4], 383-6. 98.

Currey, J. D. Physical characteristics affecting the tensile failure properties of compact bone. J.Biomech. 23[8], 837-844. 90.

Deng, Yih-Charng and Chang, Fred. Development of a finite element human thorax model. F8B. 00. GM North America Car Group.

DuBay, D. K. and Bir, C. A. Injury Risk Assessment of Single Target and Area Fire Less Lethal Munitions. ADA351554. 98. Defense Technology Corp., Casper, WY. 1998. 7p.

Dunn, M. G. and Silver, F. H. Viscoelastic behavior of human connective tissues: relative contribution of viscous and elastic components. Connect Tissue Res 12[1], 59-70. 83.

Estivalezes, E., Couteau, B., and Darmana, R. 2D calculation method based on composite beam theory for the determination of local homogenised stiffnesses of long bones. J.Biomech. 34[2], 277-283. 01.

Farshad, M., Barbezat, M., Flueler, P., Schmidlin, F., Graber, P., and Niederer, P. Material characterization of the pig kidney in relation with the biomechanical analysis of renal trauma. J.Biomech. 32[4], 417-425. 99.

Fung, Y. C. Biomechanics Mechanical Properties of Living Tissues. Second, 256. 93. Springer.

Gilbertson, Lars George. Mechanisms of fracture and biomechanics of orthoses in thoracolumbar injuries. 93.

Goldstein, S. A., Matthews, L. S., Kuhn, J. L., and Hollister, S. J. Trabecular bone remodeling: an experimental model. J.Biomech. 24 Suppl 1, 135-150. 91.

Gordon R.Plank, Michael Kleinberger, and Rolf H.Eppinger. Analytical investigation of driver thoracic response to out of position airbag deployment. SAE Stapp Car Crash Conference Proceedings 983165. 98.

Hodgskinson, R. and Currey, J. D. The effect of variation in structure on the Young's modulus of cancellous bone: a comparison of human and nonhuman material. Proc Inst.Mech.Eng [H.] 204[2], 115-121. 90.

Kaneko, T. S., Pejcic, M. R., Tehranzadeh, J., and Keyak, J. H. Relationships between material properties and CT scan data of cortical bone with and without metastatic lesions. Med.Eng Phys. 25[6], 445-454. 03.

Keyak, J. H. and Rossi, S. A. Prediction of femoral fracture load using finite element models: an examination of stress- and strain-based failure theories. J.Biomech. 33[2], 209-214. 00.

Klinger, David and Hubbs, Ken. Citizen Injuries from law enforcement impact munitions: evidence from the field. Journal of the International Wound Ballistics Association 4[4], 9-30. 00.

Kroell, Charles K., Allen, Stanley D., Warner, Charles Y., and Perl, Thomas R. Interrelationship of Velocity and Chest Compression in Blunt Thoracic Impact to Swine Ii. Proceedings - Society of Automotive Engineers P-189.Publ by SAE, Warrendale, PA, USA , 99-121. 81.

Lau, Ian V. and Viano, David C. Viscous Criterion - Bases and Applications of an Injury Severity Index for Soft Tissues. Proceedings - Society of Automotive Engineers P-189.Publ by SAE, Warrendale, PA, USA , 123-142. 86.

Lee, M., Kelly, D. W., and Steven, G. P. A model of spine, ribcage and pelvic responses to a specific lumbar manipulative force in relaxed subjects. J Biomech 28[11], 1403-8. 95.

Liu, Z. and Bilston, L. On the viscoelastic character of liver tissue: experiments and modelling of the linear behaviour. Biorheology 37[3], 191-201. 00.

Liu, Z. and Bilston, L. E. Large deformation shear properties of liver tissue. Biorheology 39[6], 735-742. 02.

Lizee, Emmanuel, Stéphane Robin, Eric Song, Nicolas Bertholon, Jean-Yves Le Coz, Benoît Besnault, and François Lavaste. Development of a 3D finite element model of the human body. SAE Stapp Car Crash Conference Proceedings 983152. 98.

Lyon, D. H., Bir, C. A., and Patton, B. J. Injury Evaluation Techniques for Non-lethal Kinetic Energy Munitions. ARL-TR-1868. 99. Army Research Laboratory, January 1999.

Mahajna, A., Aboud, N., Harbaji, I., Agbaria, A., Lankovsky, Z., Michaelson, M., Fisher, D., and Krausz, M. M. Blunt and penetrating injuries caused by rubber bullets during the Israeli-Arab conflict in October, 2000: a retrospective study. Lancet 359[9320], 1795-1800. 02.

Miller, C. E., Vanni, M. A., and Keller, B. B. Characterization of passive embryonic myocardium by quasilinear viscoelasticity theory. J.Biomech. 30[9], 985-988. 97.

Miller, K. Constitutive modelling of abdominal organs. J.Biomech. 33[3], 367-373. 00.

Miller-Young, J. E., Duncan, N. A., and Baroud, G. Material properties of the human calcaneal fat pad in compression: experiment and theory. J.Biomech. 35[12], 1523-1531. 02.

Minotti, P. and Lexcellent, C. Geometric and kinematic modelling of a human costal slice. J Biomech 24[3-4], 213-21. 91.

Patrick, L. M. and Levine, R. S. Injury to Unembalmed Belted Cadavers in Simulated Collisions. Proceedings of Stapp Car Crash Conference , 79-115. 75.

Patwardhan, A. G., Li, S. P., Gavin, T., Lorenz, M., Meade, K. P., and Zindrick, M. Orthotic stabilization of thoracolumbar injuries. A biomechanical analysis of the Jewett hyperextension orthosis. Spine 15[7], 654-661. 90.

Reilly, D. T. and Burstein, A. H. The elastic and ultimate properties of compact bone tissue. J Biomech 8[6], 393-405. 75.

Rho, J. Y., Hobatho, M. C., and Ashman, R. B. Relations of mechanical properties to density and CT numbers in human bone. Med.Eng Phys. 17[5], 347-355. 95.

Roberts, Sanford B. and Chen, P. H. Global Geometric Characteristics of Typical Human Ribs. Journal of Biomechanics v 5[n 2], 191-201. 72.

Ryan, S. D. and Williams, J. L. Tensile testing of rodlike trabeculae excised from bovine femoral bone. J.Biomech. 22[4], 351-355. 89.

Schultz, Albert B., Benson, Daniel R., and Hirsch, Carl. Force-Deformation Properties of Human Ribs. Journal of Biomechanics v7[n 3], 303-309. 74.

Shank, Ellsworth B. A Comparison of Various Less Lethal Projectiles. AD-785509. 74.

Shen, Weixin, Eugene Niu, and Stuhmiller, James H. Behind Armor Blunt Trauma Assessment: 2003 Annual Report. J3150-20-03-196. 03.

Silver, F. H., Freeman, J. W., and DeVore, D. Viscoelastic properties of human skin and processed dermis. Skin Res.Technol. 7[1], 18-23. 01.

Steele, J. A., McBride, S. J., Kelly, J., Dearden, C. H., and Rocke, L. G. Plastic bullet injuries in Northern Ireland: experiences during a week of civil disturbance. J.Trauma 46[4], 711-714. 99.

Stuhmiller, J. H., Kan, Kit K., and Ho, Kevin H. H. Interim Total Body Model: A Model of Impact Injury. J2997.43-00-107. 96.

Taylor, W. R., Roland, E., Ploeg, H., Hertig, D., Klabunde, R., Warner, M. D., Hobatho, M. C., Rakotomanana, L., and Clift, S. E. Determination of orthotropic bone elastic constants using FEA and modal analysis. J.Biomech. 35[6], 767-773. 02.

Truong, X. T. Viscoelastic wave propagation and rheologic properties of skeletal muscle. Am J Physiol 226[2], 256-64. 74.

Truong, X. T., Jarrett, S. R., and Nguyen, M. C. A method for deriving viscoelastic modulus for skeletal muscle from transient pulse propagation. IEEE Trans Biomed Eng 25[4], 382-4. 78.

Van Rietbergen, B., Weinans, H., Huiskes, R., and Odgaard, A. A new method to determine trabecular bone elastic properties and loading using micromechanical finite-element models. J.Biomech. 28[1], 69-81. 95.

Viano, David C. and Lau, Ian V. Viscous Tolerance Criterion for Soft Tissue Injury Assessment. Journal of Biomechanics 21[5], 387-399. 88.

Weiss, Jeffrey A., Maker, Bradley N., and Govindjee, Sanjay. Finite element implementation of incompressible, transversely isotropic hyperelasticity. Computer Methods in Applied Mechanics & Engineering 135[1-2 Aug 15], 107-128. 96.

Yamada, Hiroshi. Strength of Biological Materials. 297. 70. Baltimore, The Williams & Wilkins Company. Evans, F. G.